APPLICATION AND CHARACTERIZATION OF ENERGY DEPOSITION IN HIGH SPEED FLOW CONTROL

BY MONA GOLBABAEI-ASL

A dissertation submitted to the

Graduate School—New Brunswick

Rutgers, The State University of New Jersey

In partial fulfillment of the requirements

For the degree of

Doctor of Philosophy

Graduate Program in Mechanical and Aerospace Engineering

Written under the direction of

Doyle D. Knight

And approved by

_____

_____

_____

_____

New Brunswick, New Jersey

October, 2014

ABSTRACT OF THE DISSERTATION

Application and Characterization of Energy Deposition in High Speed Flow Control

By MONA GOLBABAEI-ASL

Dissertation Director:

Doyle D. Knight

Energy deposition is a robust technique for various high speed flow control applications including drag reduction. A numerical study is performed for perfect gas flow approaching a blunt cylinder at Mach 3. The energy deposition is simulated by a high temperature filament injected in front of the cylinder. The effect of important dimensionless parameters is studied to characterize the drag modification. The results indicate a saturation effect on maximum drag reduction at higher magnitudes of energy deposition. The computations reveal that the discharge location of the filament does not significantly impact the drag. A phenomenological examination of the interaction is performed. The effectiveness and efficiency of the filament on drag reduction are investigated. A one-dimensional analytical approach is studied to describe the numerical results.

Acknowledgements

It is with immense gratitude that I acknowledge my adviser Professor Doyle Knight whose support with my thesis was endless. I owe the completion of my degree to his consideration on my academic requirements. During the past years, his attitude has continually conveyed a spirit of excitement in regard to research and teaching. I wish to thank his guidance, patience, and attention.

Besides my adviser, I would like to thank my committee members professor Prosejit Bagchi and Professor Hao Lin from the Department of Mechanical and Aerospace Engineering, and Professor Gerard Richter from the Department of Computer Science.

It also gives me pleasure to thank all the staff and colleagues in the Department of Mechanical and Aerospace Engineering. My special gratitude goes to Carmen, Cindy, and Shefali. I would like to thank the computer support by Alexei Kotelnikov and Robert Perez.

This thesis would not have been possible unless for the scholarships I have received from Rutgers Engineering School and Zonta International Organization.

The research findings in this dissertation are published in more details in Shock Waves Journal.

Foremost, I would like to express my gratitude to God in the first place and then to my parents Minoo and Dariush Golbabaei and to my sister Sanaz Golbabaei for all their support, concern, kindness, and encouragement.

Dedication

To Sanaz

Table of Contents

List of Tables

List of Figures

List of Abbreviations

c_p = specific heat at constant pressure
c_v = specific heat at constant volume
C_D = drag coefficient
ΔT = maximum added temperature to filament
D = cylinder diameter
d = high temperature filament diameter
e = energy per unit mass
L = cylinder length
M = Mach number
p = pressure
Q = energy deposited to filament
$\mathcal{Q}$ = flux vector
R = gas constant
T = temperature
t = time
u = velocity
V = filament volume
v = velocity
δ = shock stand-off distance; relative error
ϵ = dimensionless energy deposition
η = efficiency parameter
γ = specific heat ratio
ρ = density
τ = dimensionless time
ζ = effectiveness parameter
τ = dimensionless time

subscripts

∞ = upstream properties
f = property at end of filament interaction
t = total property
i = specific grid property
o = initial property
s = steady state property

superscripts

$\rightarrow$ = vector
$\bar{}$ = time average
$'$ = property at time of filament initialization
$''$ = property after initialization of filament

Chapter 1

Introduction

1.1 Motivation and Background

There are many challenges associated with design of supersonic air vehicles including efficiency, performance, sonic boom and environmental issues. Due to the extreme flight conditions in the supersonic regime, the application of conventional devices to overcome these design issues may not be effective. One of the major problems with supersonic aircraft is the existence of shock waves whereby wave drag is generated. High drag impacts the fuel efficiency significantly. Therefore, it is of great importance to find innovative methods of flow control for drag reduction.

Over the past several decades energy deposition has been recognized as a modern and robust method for a variety of flow control applications including maneuvering and drag reduction [1, 2, 3, 4, 5, 6]. Energy deposition can be attained by several means including laser and/or microwave discharge. In particular, the method can have a dual application in design of supersonic vehicles which require maneuverability as well as drag mitigation. Due to the small characteristic timescales of high speed flow, application of conventional electromechanical devices is practically inefficient for rapid maneuvering purposes due to their comparably slow actuation times relative to the flowfield timescales. In contrast, energy deposition benefits from a virtually instantaneous actuation time [1]. Therefore, energy deposition may be highly practical for drag reduction purposes in supersonic flows.

Energy deposition by laser and/or microwave discharge generates a high pressure and temperature plasma region ("plasmoid"). A blast wave forms and propagates from the plasma region into the flowfield with the expansion waves reflecting back. The expansion waves lead to a rarefied region and its interaction with the shock system generates a baroclinic toroidal vortex [7] which alters the aerodynamic properties [4] and reduces drag [8].

1.2 Literature Review

1.2.1 Laser Energy Deposition in Quiescent Air

Experimental and numerical studies have been focused on laser energy deposition in air and other transparent media to examine the filamentation features and gas dynamics effects [9, 10, 11, 12]. Yan et al. [10] used two ND:YAG lasers. The first laser with a power of 500 mJ was used to create a laser sheet. The second laser with a power of 180 mJ was used to create a 10 ns discharge to a focal volume on the previously generated sheet. The blast wave from the laser breakdown and flow regimes at different time intervals after the discharge were visualized by Rayleigh scattering (RS) technique (Figure 1.1). An ellipsoidal blast wave is generated immediately after discharge which becomes spherical as it moves outward into the air. In addition, a plasma region forms at the point of discharge which creates a detonation wave. The detonation wave moves up towards the focal lens. The cool air moves into the back of the plasma. Later to the discharge, a vortex ring also forms due to the detonation wave and the asymmetric process. The size, shape, and asymmetry values depend on the energy deposition magnitudes (Figure 1.1). In addition, a perfect gas numerical simulation was performed to present a gas dynamics model for the laser discharge. Based on the magnitude of the deposited energy, an approximate initial temperature profile was introduced inside the laser induced plasma region. The numerical model was capable of predicting the shock wave profile within 5% of the experimental results.

Couairon and Mysyrowicz [12] conducted an extensive research on femtosecond laser filamentation in different transparent non-linear and dispersive media with an emphasis on air. Figure 1.2 presents the propagation of an 800 nm laser beam in the Laboratory of Applied Optics at École Polytechnique with the a hot core of diameter ~ 100 μm and an electron plasma density of $\sim 5 \times 10^{13}$ W/cm^2. Theoretical models were presented for femtosecond filamentation to develop an evolution equation in terms of the power and beam width. The applications of femtosecond laser in solids, atmosphere, lightning protection, virtual antenna, propulsion, and power supply of high speed electric vehicles were studied. They showed that depending on the application, filamentations with different plasma column length, laser intensity, and ionization track is required. Figure 1.3 shows the cross

sectional features of a laser filamentation at different propagation distances [13, 12]. Figure 1.4 shows different propagation distances with different discharge times [11, 12].

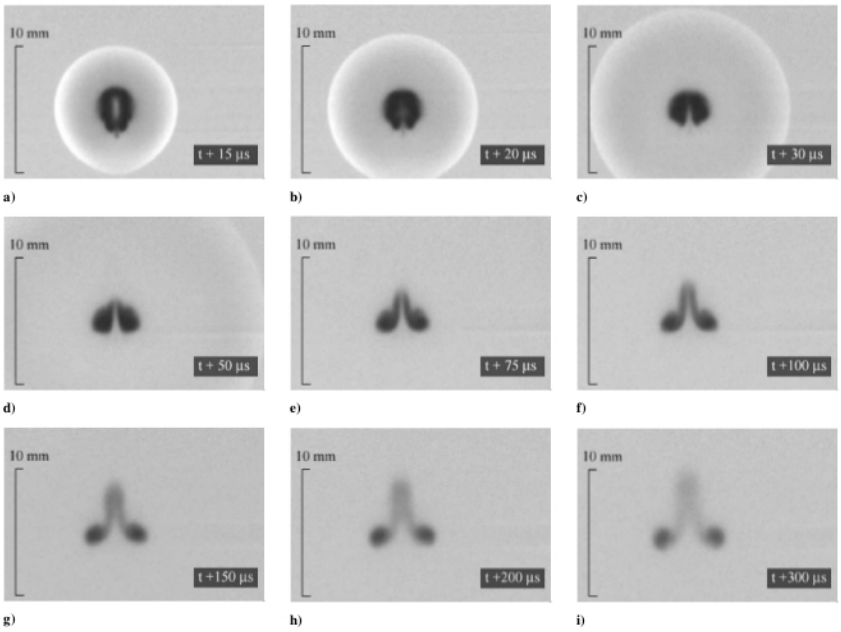

Figure 1.1: The flow regime at different time intervals subsequent to laser discharge [10]

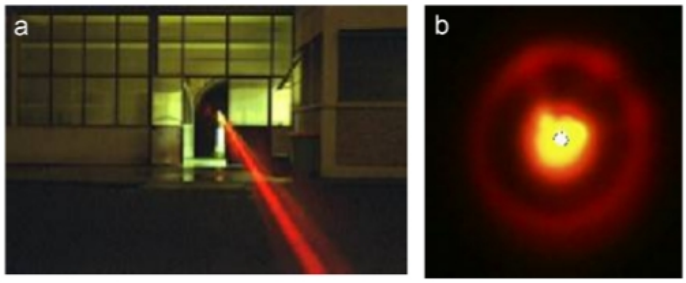

Figure 1.2: Laser beam (800 nm) generated at the Laboratory of Applied Optics at École Polytechnique, Palaiseau [12]

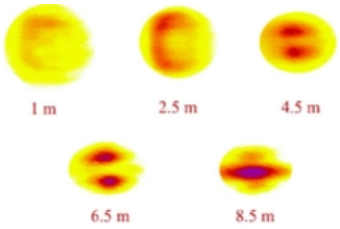

Figure 1.3: Formation of twin filaments created by laser discharge (800 nm, 50 fs, and 5 mJ) and the transverse section of the beam at different propagation distances [13, 12]

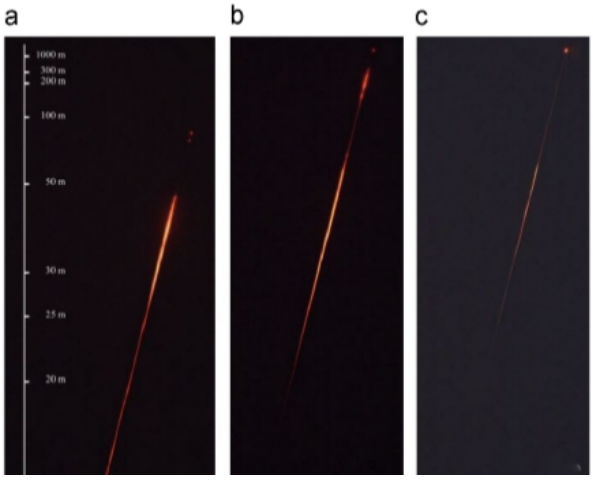

Figure 1.4: Propagation distance with different laser pulse durations: a) 100 fs, b) 1 ps, and c) 2 ps. [11, 12]

1.2.2 Microwave energy Deposition in Quiescent Air

Microwave energy deposition has been studied both numerically and experimentally. Khmara et al. [14] have investigated the temperature increase by a microwave discharge of 9 GHz in air which is initially at a temperature of 200 K and a pressure of 70 Torr. A simplified kinetic model was run by two independent codes. The results from the numerical simulation for the gas temperature were in agreement with the measured magnitudes within 10 K.

Kolesnichenko [15] performed numerous experiments for different gases at different pressures with different discharge energies and durations. He observed different shapes of microwave discharges and categorized the discharge into three types of continuous, with curved channels, and with straight channels (Figure 1.5). He also provided a curve to distinguish

microwave discharge types based on discharge and gas parameters.

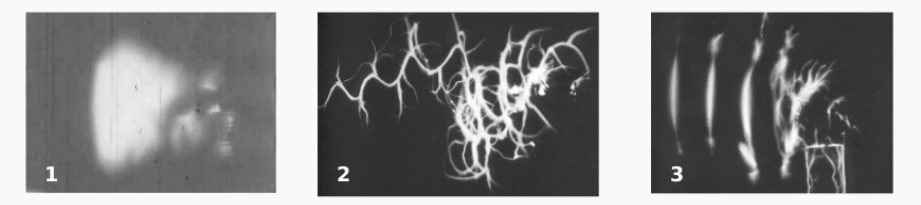

Figure 1.5: Microwave discharge types: 1) continuous, 2) with curved channels, and 3) with straight channels [15]

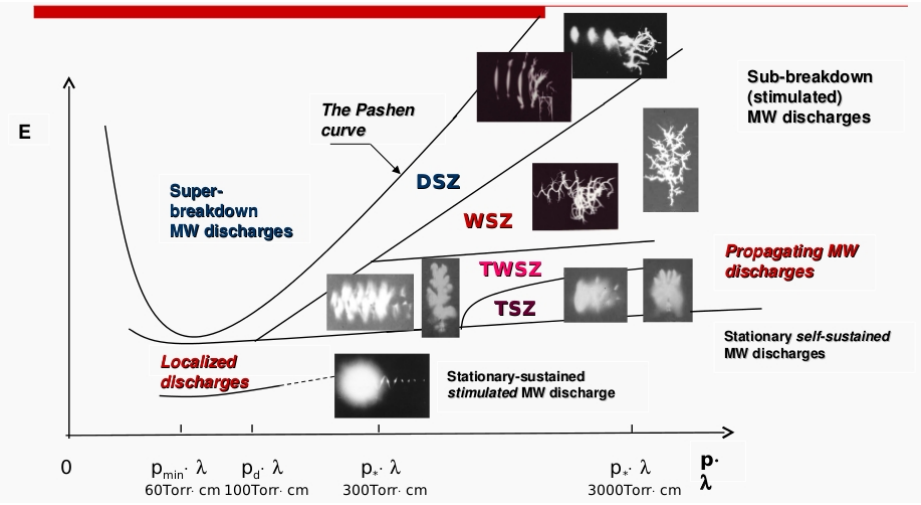

Figure 1.6: Types of microwave discharge for single pulse [15]

1.2.3 Combined Laser and Microwave Energy Deposition in Quiescent Air

Recently, the combination of laser and microwave discharge has received attention. In contrast to single laser or microwave discharge, this type of discharge enables generation of plasmoids with repeatable specified geometric shapes with less powers [16, 17, 18, 19, 20]. Bodrov et al. [19] designed an experimental setup to generate a plasma filament with combined discharge (Figure 1.7). A plasma channel is initially generated by the laser discharge and acts like a one-wire line which the electromagnetic wave can propagate through (Figure 1.8). It was seen that compared to single microwave discharge, the laser radiation initiation was able to reduce the required electric field power by a factor of two. In addition, the

time of the existence of the initial plasma was dependent on the duration of the microwave discharge.

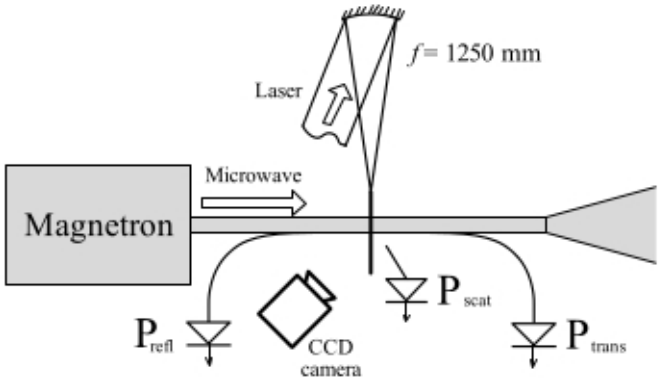

Figure 1.7: Schematics of the experimental setup to generate combined laser and microwave discharge [19]

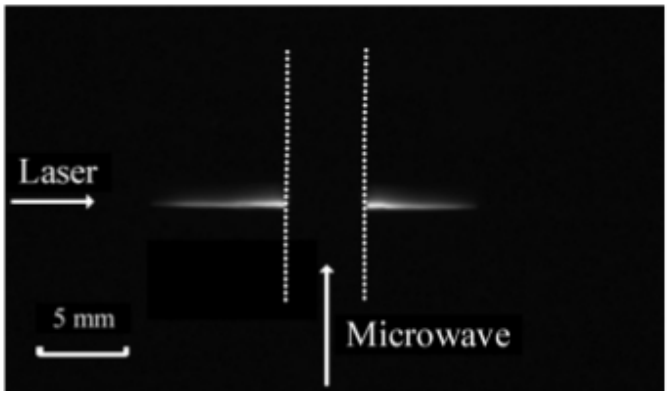

Figure 1.8: Laser radiation prior to the electromagnetic wave discharge through the waveguide [19]

1.2.4 Laser Energy Deposition for Flow Control

Experimental and computational studies have examined the effect of a laser discharge on the flowfield of a simplified aerodynamic shape [21, 22, 23, 24, 25, 26, 27, 28, 29, 30, 31, 32]. Adelgren et al. [26] conducted experiments to investigate the effect of a single pulse laser discharge on shock wave structure and surface pressure in flow past a sphere at Mach 3.45 and observed a momentary 40% decrease in surface pressure. Sasoh et al. [28] performed experiments to study the effect of ambient pressure on the interaction of a shock wave

and focused laser plasma bubble. It was seen that the vortex structure formed due to baroclinic effect was self-similar with respect to the pressure ratios of deposited energy and ambient air. Fornet et al. [30] numerically found a 21% drag reduction for an on-axis thin cylindrical discharge ahead of a axisymmetric quasi-realistic nose at Mach 3. Kandala and Candler [29] performed a numerical investigation of local instantaneous energy deposition in supersonic flow past a sphere which resulted in an instantaneous heat transfer decrease and a longer drag reduction effect. Rogier et al. [31] performed a numerical modeling of a supersonic nose cone and an instantaneous laser-induced thin cylindrical plasma in the front which lead into a momentary 18% drag decrease. Schulein et al. [32] performed an experimental investigation of a single and double-pulsed laser induced energy discharge upstream of a sphere at Mach 3.45 and examined the deformation of the bow shock and the effect on drag. The tests showed the formation of a secondary flow jet and in the case of the double-pulse laser-induced plasma the jet was accelerated due to vorticity generation as a result of the blast wave from the second pulse penetrating into the neighboring discharge. The test results indicated the location and the power of the energy source solely affect the peak times on the drag diagram. In addition, they observed that the energy deposition becomes ineffective when the source is very close to the sphere. Girgis et al. [27] performed a parametric study for a cone at different Mach numbers with an off-axis heat source upstream. A perfect gas mode was incorporated to optimize the steering forces and drag reduction, the source location and power effect were investigated.

1.2.5 Microwave Energy Deposition for Flow Control

Experimental and computational studies have also examined the effect of a microwave discharge on the flowfield of a simplified aerodynamic shape [33, 34, 35, 36, 37, 38, 39, 40]. Exton et al. [33] have shown experimentally that for a microwave-generated plasma upstream of a bow shock at Mach 6, a sufficient increase in spatial and temporal size of the plasma is required to make it effectively interact with bow shock. Lashkov et al. [36] performed experiments to study the interaction of a microwave discharge with the flowfield corresponding to different aerodynamic body shapes resulting in drag reduction. Knight et al. [37] developed a real gas model and studied the interaction of microwave-induced plasma with the shock

wave generated by a hemisphere cylinder at Mach 2.1 and showed close agreement with the experimental surface pressure measurements. Azarova et al. [34, 38, 39] performed an extensive study on introduction of rarefied filaments on- and off-axis upstream of blunt and pointed bodies in planar and cylindrical configurations with perfect gas assumption. Two general types of small and large scaled fluctuations was observed in the flowfield for different filament diameters. In addition, cases of finite and infinite filaments with steady and periodic addition were studied. Computations were completed for different Mach numbers, off-axis locations, body diameters and density ratios. Drag and lift force (off-axis filament) were calculated for all configurations and the flow structure was investigated. In a similar study, Anderson and Knight [40] carried out an ideal gas numerical simulation for different lengths of heated filaments approaching a cylinder periodically at various frequencies. It was shown that the drag was effectively reduced while there was no adverse effect on heat transfer to the cylinder.

1.2.6 Combined Laser and Microwave Energy Deposition for Flow Control

Recent interest has focused on the use of combined laser and microwave discharge to generate plasmoids with repeatable specified geometric shapes to customize their interaction with the shock system of an aerodynamic body, and to reduce the power required for microwave discharge [5, 41, 19, 20]. Experiments by Brovkin et al. [41] point out the possibility of adjustment of the process of energy deposition by means of change of the delays, and also intensity levels of the microwave and laser radiation. This technique may be used to create spatially compact microwave discharges with predictable shape and position for aerodynamic applications. Kolesnichenko et al. [17, 18] performed an extensive numerical and experimental study to investigate the specifications of a laser pulsed plus microwave discharged plasma. Fomin et al. [5] have performed an extensive study on flow control applications of microwave radiation in combination with laser discharge as an effective way of creating high-power plasmas in specified geometric shapes.

1.2.7 Other Numerical Simulations of Energy Deposition for Flow Control

Numerical models have been developed to simulate the plasma region regardless of the discharge type [42, 43, 44, 45, 46, 10, 47, 48, 30]. The aerodynamic effect of the interaction of the plasmoid with the shock system is principally thermal and depends on the heating of the gas by the discharge [44]. Thus, a simple perfect gas assumption can provide sufficiently accurate results, noting, however, that the fraction of energy of the discharge which results in heating of the gas (*i.e.,* increasing the translational-rotational temperature) must either be assumed or determined from experiment [10]. Georgievsky and Levin [42, 46, 47] studied bow shock structures and drag coefficient for different body shapes affected by both single and pulsed periodic energy source upstream. The results indicated the occurrence of irregular flow with smaller radii of source with the same rate of energy deposited in flow. Kremeyer et al. [48] performed a series of computations for instantaneous on-axis energy deposition in supersonic/hypersonic flows approaching a cone with different angles and observed a highest drag reduction of 96%.

1.3 Objective

The objective of this paper is to characterize the interaction of a custom-shaped plasmoid, assumed to be generated instantaneously by a combined laser plus microwave discharge, on a blunt cylinder at Mach 3. The discharge is modeled as an instantaneous addition of energy in a thin cylindrical region on the cylinder axis for perfect gas flow. The filament is initialized by a high temperature profile. A dimensionless parametric study is conducted to explore the effect of temperature, length, and position of the heated filament on the maximum drag reduction and pulsating effect as well as the efficiency and effectiveness of the energy deposition system. An analytical approach is pursued to describe the numerical results for drag reduction with higher filament temperatures.

Chapter 2

Problem Statement

2.1 Problem Idealization

Incoming flow at Mach 3 is approaching a cylinder. The problem is considered axisymmetric. A wave drag is generated on the front face of the cylinder due to the formation of the bow shock upstream of the cylinder. A plasma filament is inserted instantaneously by a laser plus microwave discharge on the axis of the cylinder. The schematic of the problem is presented in Figure 2.1. The filament can be added adjacent to the front face so that it intersects the bow shock (Figure 2.1(a)) or upstream of the bow shock (Figure 2.1(b)).

A perfect gas flow is assumed. The thermal effect plays the main role in shock wave mitigation and flow control in the energy deposition method [44, 35]. Hence, the energy addition to the plasma filament is ideally simulated by a thin cylindrical high temperature filament. We are interested in the effect of energy deposition on drag. For blunt bodies, drag is primarily due to fluid pressure (not viscous shear) and thus we neglect viscosity effects. Therefore, the flow is inviscid and non-heat conducting.

2.2 Dimensional Analysis

Main Dimensionless Parameters

The problem is defined by five dimensionless parameters: 1) Mach number, 2) filament length to cylinder diameter ratio, 3) energy deposition parameter, 4) filament diameter to cylinder diameter ratio, and 5) specific heat ratio. The dimensionless parameters are listed in Table 2.1.

The computations are performed for $\frac{L}{D} = 1.0, 2.0, 3.0, 4.0, 5.0$ when $\frac{\Delta T}{T_\infty} = 1.0$ and for $\frac{\Delta T}{T_\infty} = 1.0, 3.0, 5.0, 7.0, 9.0, 11.0$ when $\frac{L}{D} = 4.0$. The location of the heated filament with

respect to position of the bow shock is another parameter that will be examined in the current study.

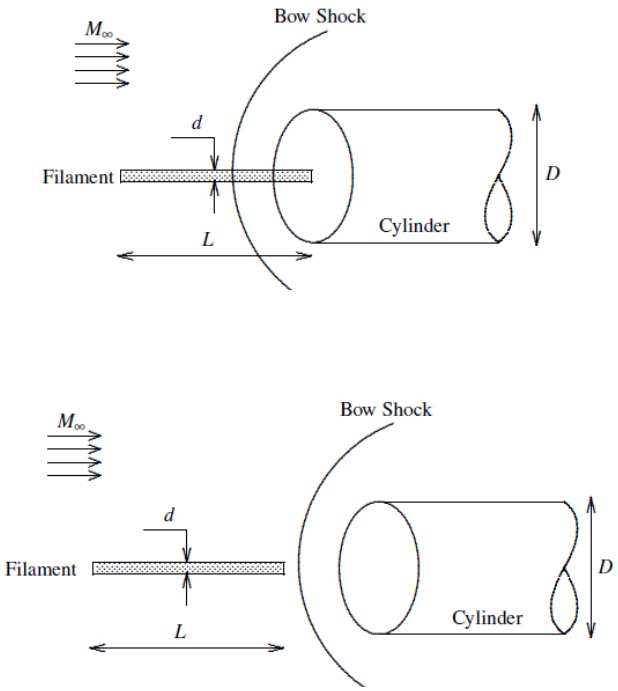

Figure 2.1: Initialization of high temperature filament (a) filament intersecting shock [1][8] (b) filament upstream the shock

Table 2.1: Dimensionless Parameters

Definition	Description	Values
M_∞	Mach Number	3
$\frac{L}{D}$	filament length to cylinder diameter ratio	$1.0, 2.0, 3.0, 4.0, 5.0$
$\frac{\Delta T}{T_\infty}$	energy deposition parameter*	$1.0, 3.0, 5.0, 7.0, 9.0, 11.0$
$\frac{d}{D}$	filament diameter to cylinder diameter ratio	0.2
γ	specific heat ratio	1.4

* see Sect. 3.4

[1]Figure reprinted with permission of the American Institute of Aeronautics and Astronautics

Chapter 3

Governing Equations, Configuration, Boundary and Initial Conditions

3.1 Governing Equations

The governing equations are the unsteady Euler equations for axisymmetric flow

$$\frac{\partial \rho}{\partial t} + \frac{1}{r}\frac{\partial \rho u_r r}{\partial r} + \frac{\partial \rho u_z}{\partial z} = 0 \tag{3.1}$$

$$\frac{\partial \rho u_r}{\partial t} + \frac{1}{r}\frac{\partial \rho u_r^2 r}{\partial r} + \frac{\partial \rho u_r u_z}{\partial z} = -\frac{\partial p}{\partial r} \tag{3.2}$$

$$\frac{\partial \rho u_z}{\partial t} + \frac{1}{r}\frac{\partial \rho u_r u_z r}{\partial r} + \frac{\partial \rho u_z^2}{\partial z} = -\frac{\partial p}{\partial z} \tag{3.3}$$

$$\frac{\partial \rho e}{\partial t} + \frac{1}{r}\frac{\partial (\rho e + p) u_r r}{\partial r} + \frac{\partial (\rho e + p) u_z}{\partial z} = 0 \tag{3.4}$$

where e, u_r, and u_z are energy per unit mass per unit volume, radial and axial velocities, respectively. The perfect gas relation is incorporated for the flowfield

$$p = \rho R T \tag{3.5}$$

3.2 Configuration

Figure 3.1 presents the schematic of the cylinder and the heated filament in the computational flow domain. The entire flow domain is axisymmetric. Therefore, it is sufficient to compute a small wedge to minimize computational cost. To compute the flow domain

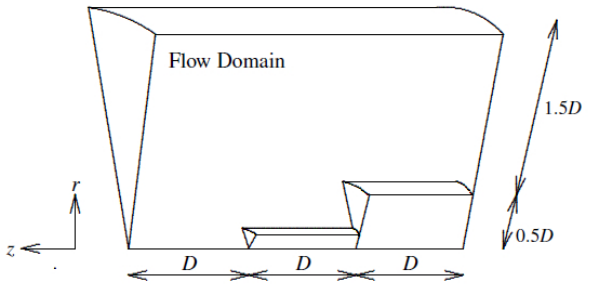

Figure 3.1: Schematic of the computational domain for $\frac{L}{D} = 1.0$

including the cylinder and the heated filament, a structured grid is generated in ICEM CFD [49].

3.3 Boundary Conditions

A supersonic inflow boundary is considered on the front (inlet) face of the flow domain. A zero-gradient boundary is applied to the downstream boundary where the flow is supersonic. A free-slip wall is considered for the far field on the top of the domain. The symmetry boundary condition is applied on each side of the domain wedge. A free-slip condition is applied to the cylinder surface.

3.4 Initial Conditions

The filament is introduced to the converged steady state solution, *i.e.*, in presence of the bow shock. The new static temperature distribution is defined by [50]

$$T(r,z) = T_s(r,z) + \Delta T e^{-(r/r_\circ)^2} \tag{3.6}$$

where

$$0 \leq r \leq r_\circ \tag{3.7}$$

where r is the radial distance in the filament, $r_\circ = d/2$ is the filament radius, $T_s(r,z)$ is the steady state temperature, and ΔT is the temperature increase due to energy deposition.

The density and the velocity vectors remain unchanged since the discharge is assumed instantaneous [29]. Likewise, the pressure is increased according to the ideal gas equation

$$p(r,z) = \rho_s(r,z)RT(r,z) \tag{3.8}$$

and therefore

$$p(r,z) = p_s(r,z) + \Delta p e^{-(r/r_\circ)^2} \tag{3.9}$$

where

$$\Delta p = \rho_s(r,z)R\Delta T \tag{3.10}$$

where ρ_s denotes the steady state density. This assumption for the initial condition is different from previous research work done by Azarova et al. [39] and Ganiev et al. [43, 45] where the pressure is considered constant and a lower density occurs inside the heated filament. In a different approach, Georgievsky and Levin [47] applied a source energy model term in the energy equation rather than initializing a temperature profile in the filament.

The change in the total energy of the flow due to the instantaneous change in temperature and pressure is

$$Q = \int_V [\rho(c_v T + \frac{1}{2}\vec{v}\cdot\vec{v}) \mid_{after} - \rho(c_v T + \frac{1}{2}\vec{v}\cdot\vec{v}) \mid_{before}] dV \tag{3.11}$$

Since ρ and $\vec{v}$ do not change,

$$Q = \int_V [\rho c_v T \mid_{after} - \rho c_v T \mid_{before}] dV \tag{3.12}$$

Substituting Equation (3.6)

$$Q = \int_V \rho_s c_v \Delta T e^{-(r/r_\circ)^2} dV \tag{3.13}$$

The initial internal energy in this volume is

$$\int_V \rho c_v T \mid_{before} dV \tag{3.14}$$

Thus, the ratio of the energy added to the filament volume to the initial internal energy in the same volume is

$$\varepsilon = \frac{Q}{\int_V \rho c_v T \mid_{before} dV} = \frac{\Delta T}{T_\infty} \frac{\int_V \rho_s e^{-(r/r_\circ)^2} dV}{\int_V \rho_s \frac{T_s}{T_\infty} dV} \tag{3.15}$$

Chapter 4

Methodology

4.1 Computational Method

The computations are performed by a finite volume code using GASPex version 5 [51]. The problem is solved in two phases. First, the steady state flow including the bow shock is converged. On the next phase, the transient simulation is carried out with the high temperature filament initialized upstream of the cylinder to investigate the interaction of the heated filament with the blunt cylinder and the consequent drag modification.

4.1.1 Grid Generation

A multiblock structured grid is generated in ICEM CFD ANSYS software for the computational domain shown in Figure 3.1. The geometry is created in ICEM CFD using CAD tools. The hexahedral elements are created using mesh tools [49]. The elements ahead of the front face of the cylinder are uniform and a boundary layer mesh is generated above the cylinder. The mesh quality tool is used to check the quality of the generated grid prior to importing to the solver. The grid specifications are given in Tables 5.1-5.3.

The grid is presented in Figure 4.1. For better visualization, some smaller cells are not shown. The grid is fine and uniform ahead of the cylinder. The cells in this location are required to be fine enough to accurately capture the heated filament interaction and to calculate the drag on the front face of the cylinder (see zone I in Figure 4.1). The cells are stretched in the radial direction in zone II using the exponential bunching tool [49]. Less number of cells are required in this region since for the current problem the physical effects are not much of interest in this area (see zone II in Figure 4.1).

To perform a grid refinement study (see sect. 5), a fine grid was initially created in ICEM

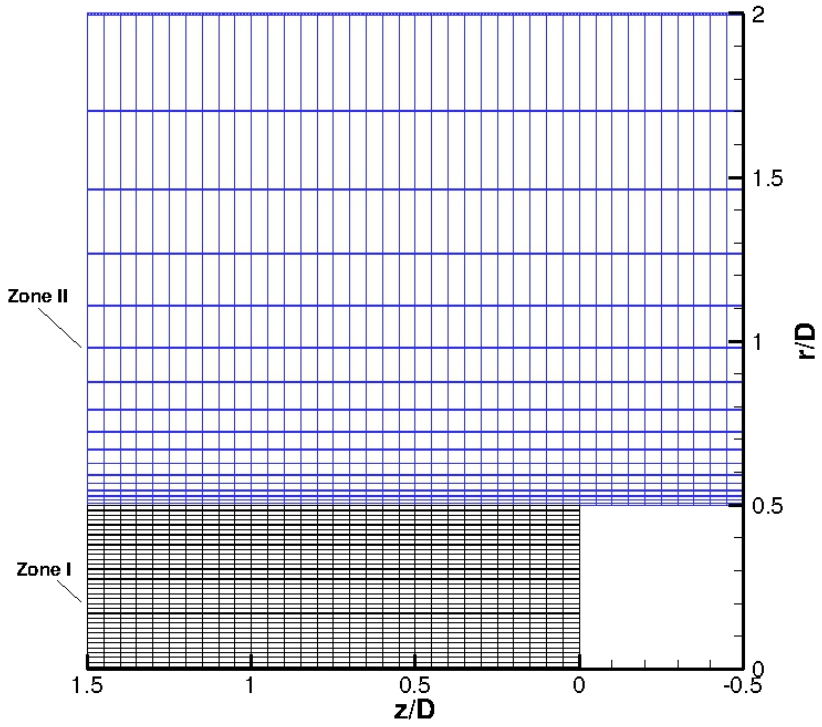

Figure 4.1: Sample grid quality for the computational domain (coarse grid)

CFD ANSYS based on which a medium and a coarse grid were generated subsequently in GASPex [51]. The sequencing process in GASPex reduces the number of nodes in radial and the axial direction in the flow domain by a factor of two at each level. This factor slightly changes in zone II due to the exponential order of the nodes (see Figure 4.1).

According to the exponential bunching rule [49]

$$S_i = S_{p,1}.i.e^{R(i-1)} \tag{4.1}$$

where S_i is the distance from the starting point on an edge to the node i, $S_{p,1}$ is spacing 1, and R is the growth ratio. Therefore [49]

$$R = \frac{-ln[(n-1).S_{p,1}]}{n-2} \tag{4.2}$$

where n is the total number of nodes on each edge. Hence, the growth ratio for the finest grid non-dimensionalized by the cylinder diameter is calculated to be 0.027 with 86 nodes along the radial direction in zone II.

4.1.2 Solution Schemes

The computations incorporate Roe's scheme with Harten modification. The temporal integration for transient analysis is explicit second-order accurate Runge-Kutta [51].

Flux Quadrature

Calculations are performed for a given number of cells according to Roe's Scheme. Roe's Scheme was developed based on the exact solution to an approximation of the general Riemann problem [52]. A similar idea was also introduced by Godunov earlier; however, Roe's Scheme does not require an iterative method to calculate the fluxes. Consider the following one-dimensional Euler equations in non-conservative differential form

$$\frac{\partial \mathcal{Q}}{\partial t} + A\frac{\partial \mathcal{Q}}{\partial x} = 0 \tag{4.3}$$

where A is the Jacobian of the flux matrix $A = \frac{\partial F}{\partial \mathcal{Q}}$ and

$$\mathcal{Q} = \left\{ \begin{array}{c} \rho \\ \rho u \\ \rho e \end{array} \right\} \tag{4.4}$$

and

$$\mathcal{F} = \left\{ \begin{array}{c} \rho \\ \rho u^2 + p \\ \rho e u + p u \end{array} \right\} \tag{4.5}$$

$$A(\mathcal{Q}) = \begin{pmatrix} 0 & 1 & 0 \\ (\gamma-3)\frac{u^2}{2} & (3-\gamma)u & \gamma - 1 \\ -Hu + \frac{(\gamma-1)u^3}{2} & H - (\gamma-1)u^2 & \gamma u \end{pmatrix} \tag{4.6}$$

where $H = e + \frac{p}{\rho}$ is the total enthalpy. Therefore, the approximate form of Euler Equations will be

$$\frac{\partial \mathcal{Q}}{\partial t} + \tilde{\mathcal{A}}(\mathcal{Q}_l, \mathcal{Q}_r)\frac{\partial \mathcal{Q}}{\partial x} = 0 \tag{4.7}$$

where $\tilde{\mathcal{A}}(\mathcal{Q}_l, \mathcal{Q}_r)$ is a constant and replaces the exact coefficient matrix in Euler Equation. The approximate matrix is calculated based on left and right values for $\mathcal{Q}$. A convenient form of the above equation for numerical calculation purpose is given by

$$F_{i+1/2} = \frac{1}{2}\left[F_l + F_r + \sum_{j=1}^{j=3} \alpha_j |\tilde{\lambda}_j| \tilde{e}_j\right] \tag{4.8}$$

where

$$\begin{aligned}
\alpha_1 &= \left[1 - \tfrac{(\gamma-1)}{2}\tfrac{\tilde{u}^2}{\tilde{a}^2}\right]\Delta\rho + \left[(\gamma-1)\tfrac{\tilde{u}}{\tilde{a}^2}\right]\Delta\rho u - \left[\tfrac{(\gamma-1)}{\tilde{a}^2}\right]\Delta\rho e \\
\alpha_2 &= \left[\tfrac{(\gamma-1)}{4}\tfrac{\tilde{u}^2}{\tilde{a}^2} - \tfrac{\tilde{u}}{2\tilde{a}}\right]\Delta\rho + \left[\tfrac{1}{2\tilde{a}} - \tfrac{\gamma-1}{2}\tfrac{\tilde{u}}{\tilde{a}^2}\right]\Delta\rho u + \left[\tfrac{(\gamma-1)}{2\tilde{a}^2}\right]\Delta\rho e \\
\alpha_3 &= \left[\tfrac{(\gamma-1)}{4}\tfrac{\tilde{u}^2}{\tilde{a}^2} + \tfrac{\tilde{u}}{2\tilde{a}}\right]\Delta\rho - \left[\tfrac{1}{2\tilde{a}} + \tfrac{\gamma-1}{2}\tfrac{\tilde{u}}{\tilde{a}^2}\right]\Delta\rho u + \left[\tfrac{(\gamma-1)}{2\tilde{a}^2}\right]\Delta\rho e
\end{aligned} \tag{4.9}$$

and the eigenvalues are given by

$$\begin{aligned}
\tilde{\lambda}_1 &= \tilde{u} \\
\tilde{\lambda}_2 &= \tilde{u} + \tilde{a} \\
\tilde{\lambda}_3 &= \tilde{u} - \tilde{a}
\end{aligned} \tag{4.10}$$

and the eigenvectors are given by

$$\begin{aligned}
\tilde{e}_1 &= \begin{Bmatrix} 1 \\ \tilde{u} \\ \frac{1}{2}\tilde{u}^2 \end{Bmatrix} \\
\tilde{e}_2 &= \begin{Bmatrix} 1 \\ \tilde{u} + \tilde{a} \\ \tilde{H} + \tilde{u}\tilde{a} \end{Bmatrix} \\
\tilde{e}_2 &= \begin{Bmatrix} 1 \\ \tilde{u} - \tilde{a} \\ \tilde{H} - \tilde{u}\tilde{a} \end{Bmatrix}
\end{aligned} \tag{4.11}$$

where

$$\tilde{u} = \tfrac{\sqrt{\rho_l}u_l + \sqrt{\rho_r}u_r}{\sqrt{\rho_l} + \sqrt{\rho_r}} \quad , \quad \tilde{H} = \tfrac{\sqrt{\rho_l}H_l + \sqrt{\rho_r}H_r}{\sqrt{\rho_l} + \sqrt{\rho_r}} \quad , \quad \tilde{a} = \sqrt{(\gamma-1)(\tilde{H} - \tfrac{1}{2}\tilde{u}^2)} \tag{4.12}$$

where $H = e + p/\rho$ and also $\Delta\rho = \rho_l - \rho_r$ and similarly for $\Delta\rho u$ and $\Delta\rho e$. Depending on the reconstruction method applied, the flux values are calculated with different accuracies. It can be shown Roe's Scheme always satisfies stability conditions [52].

4.1.3 Harten Modification

The Roe's flux-difference splitting scheme has been known to exhibit the carbuncle problem for blunt body flows. The Harten entropy fix corrects for the lack of dissipation at sonic points and at stagnation lines to prevent the carbuncle phenomenon [51]. The eigenvalues in Roe's scheme $|\tilde{\lambda}_i|$ are substituted by approximate values $|\hat{\lambda}_i|$

$$|\hat{\lambda}_i| = \begin{cases} \frac{\tilde{\lambda}_i^2}{4\varepsilon\hat{a}} + \varepsilon\hat{a} & \text{for} \quad |\tilde{\lambda}_i| < 2\varepsilon\hat{a} \\ |\tilde{\lambda}_i| & \text{for} \quad |\tilde{\lambda}_i| \geq 2\varepsilon\hat{a} \end{cases} \tag{4.13}$$

where $0 < \varepsilon \leq \frac{1}{2}$ is a positive value and $\hat{a}$ is a proper velocity scale, *e.g.* $\hat{a} = \tilde{a}$ [53].

4.1.4 The Limiter

The spatial discretization is second-order accurate with Modified ENO (Essentially Non Oscillatory) reconstruction. A reconstruction based on a symmetric stencil of cells generates unphysical extrema at discontinuities (shock waves). The ENO limiter provides a reconstruction using an asymmetric stencil of cells [52]. Therefore, a second-order reconstruction in cell i can be written as

$$\begin{aligned} \mathcal{Q}_i(x) = \quad & \mathcal{Q}_i - \frac{\left(\Delta\mathcal{Q}_{i-a+\frac{3}{2}} - \Delta\mathcal{Q}_{i-a+\frac{1}{2}}\right)}{24} \\ & + \frac{1}{\Delta x}\left[\Delta\mathcal{Q}_{i-a+\frac{1}{2}} + \left(a - \tfrac{1}{2}\right)\left(\Delta\mathcal{Q}_{i-a+\frac{3}{2}} - \Delta\mathcal{Q}_{i-a+\frac{1}{2}}\right)\right]\xi \\ & + \frac{\left(\Delta\mathcal{Q}_{i-a+\frac{3}{2}} - \Delta\mathcal{Q}_{i-a+\frac{1}{2}}\right)}{2(\Delta x)^2}\xi^2 \end{aligned} \tag{4.14}$$

where $\xi = x - x_i$. The values of a can be determined from Table 4.1.

Table 4.1: ENO Limiter: Value of a [52]

1st criterion	2nd criterion	a
$\lvert\Delta\mathcal{Q}_{i+\frac{1}{2}}\rvert \leq \lvert\Delta\mathcal{Q}_{i-\frac{1}{2}}\rvert$	$\lvert\Delta\mathcal{Q}_{i+\frac{3}{2}} - \Delta\mathcal{Q}_{i+\frac{1}{2}}\rvert \leq \lvert\Delta\mathcal{Q}_{i+\frac{1}{2}} - \Delta\mathcal{Q}_{i-\frac{1}{2}}\rvert$	0
	$\lvert\Delta\mathcal{Q}_{i+\frac{3}{2}} - \Delta\mathcal{Q}_{i+\frac{1}{2}}\rvert > \lvert\Delta\mathcal{Q}_{i+\frac{1}{2}} - \Delta\mathcal{Q}_{i-\frac{1}{2}}\rvert$	1
$\lvert\Delta\mathcal{Q}_{i+\frac{1}{2}}\rvert > \lvert\Delta\mathcal{Q}_{i-\frac{1}{2}}\rvert$	$\lvert\Delta\mathcal{Q}_{i+\frac{1}{2}} - \Delta\mathcal{Q}_{i-\frac{1}{2}}\rvert \leq \lvert\Delta\mathcal{Q}_{i-\frac{1}{2}} - \Delta\mathcal{Q}_{i-\frac{3}{2}}\rvert$	1
	$\lvert\Delta\mathcal{Q}_{i+\frac{1}{2}} - \Delta\mathcal{Q}_{i-\frac{1}{2}}\rvert > \lvert\Delta\mathcal{Q}_{i-\frac{1}{2}} - \Delta\mathcal{Q}_{i-\frac{3}{2}}\rvert$	2

In addition, GASPex reduces the reconstruction to the first order when the sign of forward and backward gradients change [51].

Temporal Quadrature

The integration of fluxes over all time steps are performed by the explicit method of second order Runge-Kutta. The equations are given by [52]

$$\begin{aligned} \mathcal{Q}_i^0 &= \mathcal{Q}_i^n \\ \mathcal{Q}_i^1 &= \mathcal{Q}_i^0 + \tfrac{\Delta t}{2} R_i^0 \\ \mathcal{Q}_i^2 &= \mathcal{Q}_i^0 + \Delta t R_1^i \\ \mathcal{Q}_i^{n+1} &= \mathcal{Q}_i^2 \end{aligned} \tag{4.15}$$

The time step size is calculated from

$$\Delta t \leq \frac{\Delta x}{\max |\lambda_i|} \tag{4.16}$$

where λ_i corresponds to three characteristics, *i.e.*, eigenvalues of $\mathcal{A}$ (see sec. 4.1.2).

$$\begin{aligned} \lambda_1 &= u \\ \lambda_2 &= u + a \\ \lambda_3 &= u - a \end{aligned} \tag{4.17}$$

where, in the current study, $\max |\lambda_i| = u + a$. Calculations are performed based on a fixed time step which is calculated initially from the initial eigenvalues (4.17). The time step values for different grids are presented in Tables 5.1-5.3.

4.1.5 Post Processing

The principal variables including geometric coordinates, thermodynamic properties, velocities, and the force on the front face of the cylinder are exported from GASPex [51]. The exported values are analyzed and processed in Tecplot to visualize different contours and graphs [54].

4.2 Analytical Method

Figure 4.2 shows the schematic of a fluid pathline behavior instantly before, at, and after initiation of the heated filament ahead of the cylinder. Location 0 represents a point on a streamline immediately upstream of the shock. Location 1 is a point downstream immediately behind the shock. Points 0, 1, and 2 lie on a single pathline. Location 2 represents a point on the front face adjacent to the corner of the cylinder. This point approximately corresponds to the sonic line in the undisturbed steady state flow which intersects the corner of the cylinder. In addition, ($'$) denotes the moment of discharge and ($''$) denotes a short time subsequent to the discharge. No symbol indicates steady state conditions prior to the filament generation. We are interested in the ratio of the disturbed to the undisturbed pressure (as an effect of the high temperature filament insertion) at point 2 on the front face of the cylinder.

4.2.1 Governing Equations: An instant prior to the addition of the heated filament

For the points 1 and 2 on the streamline adjacent to the axis, we assume a normal shock has occurred. This reduces the dimensions of the problem to one. The Rankine-Hugoniot equations hold at the steady state condition for the normal shock

$$\frac{p_1}{p_0} = 1 + \frac{2\gamma}{\gamma+1}({M_0}^2 - 1) \tag{4.18}$$

and

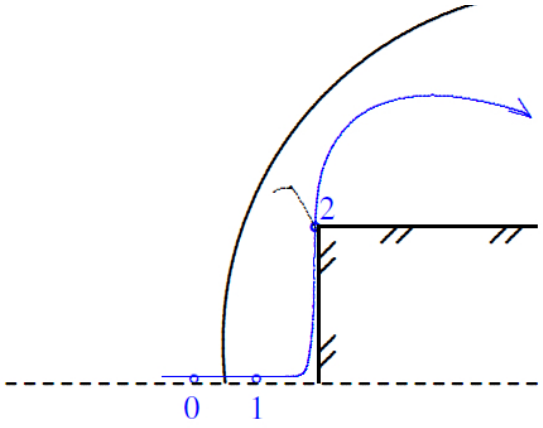

(a) An instant before initiation of heated filament

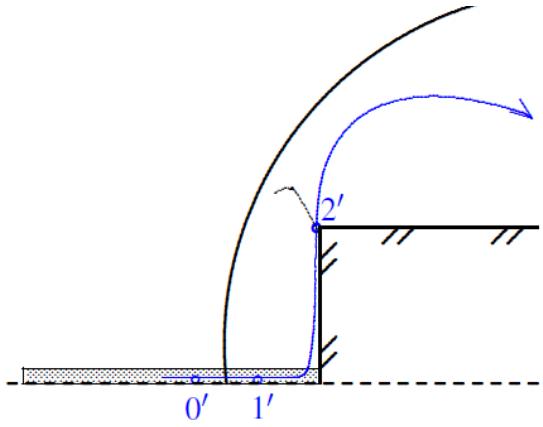

(b) At the instant of initiation of heated filament

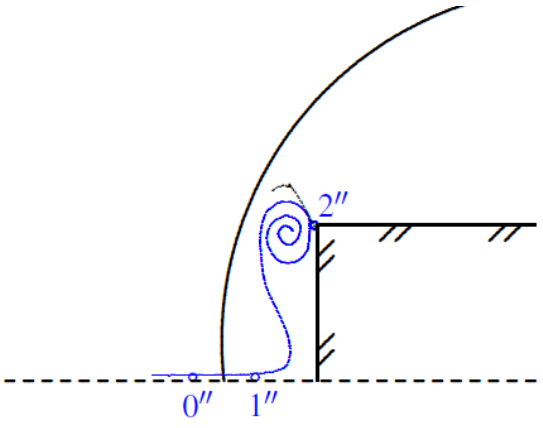

(c) An instant after initiation of heated filament

Figure 4.2: Points on a pathline adjacent to the axis of the cylinder an instant a) before, b) at, and c) after addition of high temperature filament

$$\frac{T_1}{T_0} = \frac{[2\gamma {M_0}^2 - (\gamma - 1)][(\gamma - 1){M_0}^2 + 2]}{(\gamma + 1)^2 {M_0}^2} \tag{4.19}$$

We assume an isentropic expansion process between point 1 adjacent to the axis and point 2 on the corner which approximately corresponds to the sonic line, thus

$$\frac{p_2}{p_1} = \frac{(1 + \frac{\gamma - 1}{2} M_1^2)^{\frac{\gamma}{\gamma - 1}}}{(\frac{\gamma + 1}{2})^{\frac{\gamma}{\gamma - 1}}} \tag{4.20}$$

4.2.2 Governing Equations: At the instant of addition of heated filament

The ratio $\frac{\Delta T}{T_\infty}$ represents the initial condition in the filament where the temperature profile is defined as (Figure 4.2(b))

$$T(r, z) = T_s(r, z) + \Delta T e^{-(r/r_\circ)^2} \tag{4.21}$$

and

$$0 \leq r \leq r_\circ \tag{4.22}$$

where r is the radial distance in the filament, $r_\circ$ is the filament radius, $T_s(r, z)$ is the steady state temperature, and ΔT is the temperature increase as a result of energy deposition. The density and the velocity vector are not modified by the instantaneous energy deposition. Thus, the pressure profile is given by

$$p(r, z) = p_s(r, z) + \rho_s R \Delta T e^{-(r/r_\circ)^2} \tag{4.23}$$

Therefore,

$$p_0' = p_0 + \rho_0 R \Delta T \tag{4.24}$$

and

$$T_0' = T_0 + \Delta T \tag{4.25}$$

By increasing pressure and temperature inside the filament, the shock will move upstream (lensing effect). Our computations show that the speed of the moving shock is about

20% of the freestream flow (depending on the maximum temperature increase). Therefore, as a first approximation, the shock may be considered stationary.

4.2.3 Governing Equations: An instant subsequent to the addition of the heated filament

Figure 4.2(c) presents the initiation of the recirculation region subsequent to the addition of the high temperature filament into the flowfield. A blast wave is generated shortly after the initialization of high temperature profile in the flowfield which travels from the heated filament and a series of expansion waves reflect back into the filament. We assume an isentropic expansion for the points inside the filament whereby the pressure at point 0 is reduced to the initial freestream value, *i.e.*,

$$p_0'' = p_0 \tag{4.26}$$

From isentropic flow relations

$$\frac{T_0''}{T_0'} = (\frac{p_0''}{p_0'})^{\frac{\gamma-1}{\gamma}} \tag{4.27}$$

and substituting from (4.24), (4.25), and (4.26) into (4.27)

$$\frac{T_0''}{T_0} = (1 + \frac{\Delta T}{T_0})^{\frac{1}{\gamma}} \tag{4.28}$$

Following the initiation of the filament interaction and shock stabilization, the Rankine-Hugoniot conditions hold for new values of flow properties, *i.e.*,

$$\frac{p_1''}{p_0''} = 1 + \frac{2\gamma}{\gamma+1}(M_0''^2 - 1) \tag{4.29}$$

where M_0'' is found for the new temperature value from (4.28)

$$M_0'' = \frac{U_0}{\sqrt{\gamma R T_0''}} = \frac{U_0}{\sqrt{\gamma R T_0}\sqrt{(1 + \frac{\Delta T}{T_0})^{\frac{1}{\gamma}}}} = \frac{M_0}{(1 + \frac{\Delta T}{T_0})^{\frac{1}{2\gamma}}} \tag{4.30}$$

In addition, the following holds for isentropic expanded flow at point $2''$ which approximately lies on the sonic line on the corner of the cylinder

$$\frac{p_2''}{p_1''} = \frac{(1 + \frac{\gamma-1}{2} M_1''^2)^{\frac{\gamma}{\gamma-1}}}{(\frac{\gamma+1}{2})^{\frac{\gamma}{\gamma-1}}} \tag{4.31}$$

where $M_1''^2$ is calculated from the Rankine-Hugoniot condition for stabilized shock (see section 4.2.2)

$$M_1''^2 = \frac{1 + \frac{\gamma-1}{2} M_0''^2}{\gamma M_0''^2 - \frac{\gamma-1}{2}} \tag{4.32}$$

Therefore, $\frac{p_2''}{p_2}$ represents the ideal pressure drop on the front face and can be rewritten as

$$\frac{p_2''}{p_2} = \frac{\frac{p_2''}{p_0}}{\frac{p_2}{p_0}} = \frac{\frac{p_2''}{p_1''} \cdot \frac{p_1''}{p_0''}}{\frac{p_2}{p_1} \cdot \frac{p_1}{p_0}} \tag{4.33}$$

and is calculated by substituting for $\frac{p_2''}{p_1''}$, $\frac{p_1''}{p_0''}$, $\frac{p_2}{p_1}$, and $\frac{p_1}{p_0}$ from (4.31), (4.29), (4.20), and (4.18) respectively. The result is

$$\frac{p_2''}{p_2} = \left[\frac{1 + \frac{\gamma-1}{2} M_1''^2}{1 + \frac{\gamma-1}{2} {M_1}^2}\right]^{\frac{\gamma}{\gamma-1}} \left[\frac{1 + \frac{2\gamma}{\gamma+1}(M_0''^2 - 1)}{1 + \frac{2\gamma}{\gamma+1}({M_0}^2 - 1)}\right] \tag{4.34}$$

where from (4.30)

$$M_0''^2 = \frac{{M_0}^2}{(1 + \frac{\Delta T}{T_0})^{\frac{1}{\gamma}}} \tag{4.35}$$

and $M_1''^2$ is given by (4.32). Likewise,

$${M_1}^2 = \frac{1 + \frac{\gamma-1}{2} {M_0}^2}{\gamma {M_0}^2 - \frac{\gamma-1}{2}} \tag{4.36}$$

Chapter 5

Grid Refinement Study

A grid sensitivity evaluation is performed to check the numerical accuracy of the results for the average drag reduction from each computational grid. The average drag reduction is defined as

$$\overline{\Delta C_D} = \frac{\int_0^{t_f} |C_{D_f} - C_{D_s}| dt}{t_f} \tag{5.1}$$

where C_D is

$$C_D = \frac{\int_0^{2\pi} \int_0^{D/2} [p(r) - p_\infty] r dr d\theta}{\frac{1}{2}\rho_\infty U_\infty^2 (\pi \frac{D^2}{4})} \tag{5.2}$$

where C_{Df} denotes the modified drag coefficient due to interaction of the heated filament and C_{Ds} represents the steady state drag coefficient value prior to discharge.

Two grid refinement levels are computed. In all three grid sets, the cell spacing is equal in both axial and radial directions. The specifications for the three different grid sets, *i.e.*, fine, medium, and coarse mesh are given in Tables 5.1-5.3.

The relative error for the fine grid with respect to the medium grid is

$$\delta = 100 \times \frac{\overline{\Delta C_{D,fine\,grid}}}{\overline{\Delta C_{D,medium\,grid}}} \tag{5.3}$$

The results for average drag reduction (Equation 5.1) and relative error (Equation 5.3) from all grid sets and cases are listed in Tables 5.4 (filament length study) and 5.5 (filament temperature study). The average relative error is about 2.9% which indicates reasonable grid covergence. In addition, for the steady state case, the drag coefficient results vary less than one percent between the two finer grids.

Table 5.1: Mesh specifications for coarse grid, "$\Delta s = 0.005$"*

	number of cells	number of cells	number of cells	dimensionless filament interaction time	dimensionless time step
	$r < d/2$ $0 < z < L$	$d/2 < r < D/2$	$r > D/2$	τ_f	$\Delta\tau = \frac{U_\infty}{D}\Delta t$
$\frac{L}{D} = 1.0$	$4,000$	$36,000$	$10,200$	1	2.1×10^{-3}
$\frac{L}{D} = 2.0$	$8,000$	$72,000$	$17,000$	2	2.1×10^{-3}
$\frac{L}{D} = 3.0$	$12,000$	$68,000$	$17,000$	3	2.1×10^{-3}
$\frac{L}{D} = 4.0$	$16,000$	$104,000$	$23,800$	4	2.1×10^{-3}
$\frac{L}{D} = 5.0$	$20,000$	$100,000$	$23,800$	5	2.1×10^{-3}
$\frac{L}{D} = 3.0$ upstream	$12,000$	$108,000$	$23,800$	3	2.1×10^{-3}

* cell spacing non-dimensionalized by cylinder diameter

Table 5.2: Mesh specifications for medium grid, "$\Delta s = 0.0025$"*

	number of cells	number of cells	number of cells	dimensionless filament interaction time	dimensionless time step
	$r < d/2$ $0 < z < L$	$d/2 < r < D/2$	$r > D/2$	τ_f	$\Delta\tau = \frac{U_\infty}{D}\Delta t$
$\frac{L}{D} = 1.0$	$16,000$	$144,000$	$20,400$	1	1.0×10^{-3}
$\frac{L}{D} = 2.0$	$32,000$	$288,000$	$34,000$	2	1.0×10^{-3}
$\frac{L}{D} = 3.0$	$48,000$	$272,000$	$34,000$	3	1.0×10^{-3}
$\frac{L}{D} = 4.0$	$64,000$	$416,000$	$47,600$	4	1.0×10^{-3}
$\frac{L}{D} = 5.0$	$80,000$	$400,000$	$47,600$	5	1.0×10^{-3}
$\frac{L}{D} = 3.0$ upstream	$48,000$	$432,000$	$47,600$	3	1.0×10^{-3}

* cell spacing non-dimensionalized by cylinder diameter

Table 5.3: Mesh specifications for fine grid, "$\Delta s = 0.00125$"*"

	number of cells	number of cells	number of cells	dimensionless filament interaction time	dimensionless time step
	$r < d/2$ $0 < z < L$	$d/2 < r < D/2$	$r > D/2$	τ_f	$\Delta\tau = \frac{U_\infty}{D}\Delta t$
$\frac{L}{D} = 1.0$	$64,000$	$576,000$	$204,000$	1	5.2×10^{-4}
$\frac{L}{D} = 2.0$	$128,000$	$1,152,000$	$340,000$	2	5.2×10^{-4}
$\frac{L}{D} = 3.0$	$192,000$	$1,088,000$	$340,000$	3	5.2×10^{-4}
$\frac{L}{D} = 4.0$	$256,000$	$1,664,000$	$476,000$	4	5.2×10^{-4}
$\frac{L}{D} = 5.0$	$320,000$	$1,600,000$	$476,000$	5	5.2×10^{-4}
$\frac{L}{D} = 3.0$ upstream	$192,000$	$1,728,000$	$476,000$	3	5.2×10^{-4}

* cell spacing non-dimensionalized by cylinder diameter

Table 5.4: Average drag reduction and relative error values for different grids in filament length study

	Coarse grid	Medium grid	Fine grid	Relative error
$\frac{\Delta T}{T_\infty} = 1.0$	$\Delta s = 0.005$	$\Delta s = 0.0025$	$\Delta s = 0.00125$	δ
$\frac{L}{D} = 1.0$	0.073	0.080	0.085	5.000
$\frac{L}{D} = 2.0$	0.203	0.204	0.212	3.825
$\frac{L}{D} = 3.0$	0.265	0.267	0.270	0.978
$\frac{L}{D} = 4.0$	0.314	0.317	0.331	4.190
$\frac{L}{D} = 5.0$	0.385	0.400	0.430	7.007
$\frac{L}{D} = 3.0$ upstream	0.272	0.270	0.273	1.079

Table 5.5: Average drag reduction and relative error values for different grids in filament temperature study

	Coarse grid	Medium grid	Fine grid	Relative error
$\frac{L}{D} = 4.0$	$\Delta s = 0.005$	$\Delta s = 0.0025$	$\Delta s = 0.00125$	δ
$\frac{\Delta T}{T_\infty} = 1.0$	0.314	0.317	0.331	4.190
$\frac{\Delta T}{T_\infty} = 3.0$	0.510	0.511	0.512	0.220
$\frac{\Delta T}{T_\infty} = 5.0$	0.596	0.594	0.589	0.910
$\frac{\Delta T}{T_\infty} = 7.0$	0.637	0.661	0.664	0.467
$\frac{\Delta T}{T_\infty} = 9.0$	0.691	0.720	0.743	3.101
$\frac{\Delta T}{T_\infty} = 11.0$	0.734	0.764	0.799	4.313

The fine grid results are used to demonstrate flow contours in Sect. 6. All the results in this section are computed in Matlab programming environment.

Chapter 6

Results

The computational configurations are established to characterize drag modification from three important effects: 1) filament length to cylinder diameter ratio, 2) energy deposition parameter, and 3) filament location. To study the filament length effect, five different configurations of $\frac{L}{D} = 1.0, 2.0, 3.0, 4.0, 5.0$ and a sixth case of $\frac{L}{D} = 3.0$ upstream of the bow shock for $\frac{\Delta T}{T_\infty} = 1.0$ have been computed. All other dimensionless parameters are assumed constant. To examine the flowfield response to temperature increase in the filament, a total six configurations of $\frac{\Delta T}{T_\infty} = 1.0, 3.0, 5.0, 7.0, 9.0, 11.0$ for $\frac{L}{D} = 4.0$ have been computed while all other dimensionless parameters are assumed constant.

6.1 Steady State Flowfield

Figure 6.1 represents the flowfield contours at an instant of time prior and subsequent to the initialization of high temperature filament for $\frac{L}{D} = 1.0$ and $\frac{\Delta T}{T_\infty} = 1.0$. These contour plots are qualitatively similar to all the cases of filament length and temperature. The Mach contour is shown for the converged steady state solution (Figure 6.1(a)). The results for the steady state solution can be validated by two methods: 1) shock stand-off distance from experimental results and 2) stagnation pressure on the axis behind the shock from normal shock relations.

6.1.1 Shock Stand-off Distance

The numerical shock stand off distance on the axis is measured from the contour plots for the finest grid set. The numerical stand-off distance normalized by the cylinder diameter is found to be 0.327. For a blunt cylinder and from the experimental results [55]

$$\delta = 0.386(\frac{D}{2})\exp(\frac{4.67}{{M_\infty}^2}) \tag{6.1}$$

which results in 0.324 for the current cylinder diameter and incoming flow Mach number. Therefore, the numerical results are in good agreement with the experimental result. The discrepancy between experimental and numerical stand-off distance for different grids is less than 1%.

6.1.2 Stagnation Pressure on the Axis Behind the Shock

The numerical stagnation pressure on the axis behind the shock non-dimensionalized by the freestream stagnation pressure is measured from the pressure contour plot and is 0.330. Assuming the bow shock on the axis behaves similar to a normal shock, it is possible to use the stationary normal shock relations to find the exact values of stagnation pressure on the axis behind the bow shock. The stagnation pressure upstream the shock is found from the isentropic flow relations [52]

$$p_{o\infty} = p_\infty \left[1 + \frac{\gamma - 1}{2}{M_\infty}^2\right]^{\frac{\gamma}{\gamma-1}} \tag{6.2}$$

where $p_{o\infty}$ is the upstream stagnation pressure on the axis, p_∞ is the freestream pressure, and M_∞ is the freestream Mach number.

In addition, the stagnation pressure ratio upstream and downstream the stationary normal shock is found from the following relation [52]

$$\frac{p_o}{p_{o\infty}} = \left[\frac{(\gamma+1){M_\infty}^2}{2+(\gamma-1){M_\infty}^2}\right]^{\frac{\gamma}{\gamma-1}} \left[\frac{\gamma+1}{2\gamma{M_\infty}^2-(\gamma-1)}\right]^{\frac{1}{\gamma-1}} \tag{6.3}$$

where p_o denotes the stagnation pressure downstream the normal shock. Therefore, the ratio of the stagnation pressure on the axis behind the bow shock and the freestream stagnation pressure is calculated to be

$$\frac{p_o}{p_{o\infty}} = 0.328 \tag{6.4}$$

which agrees very well with the aforementioned computational result.

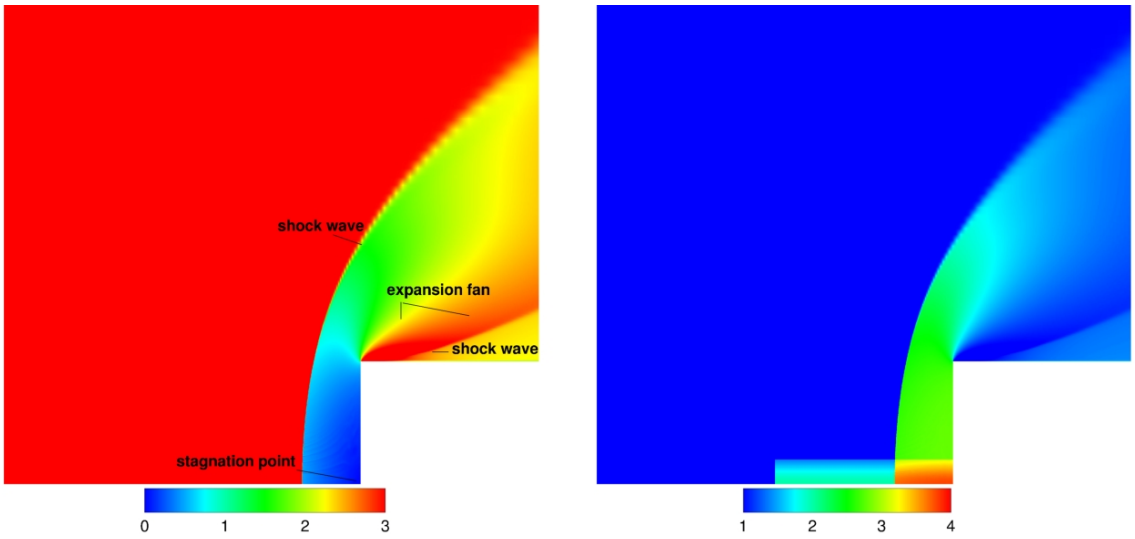

(a) Mach Number

(b) T/T_∞

Figure 6.1: Flowfield state (a) prior and (b) subsequent to the initiation of the heated filament ahead of the body ($\frac{L}{D} = 1.0$ and $\frac{\Delta T}{T_\infty} = 1.0$) [1][8]

6.2 Filament Interaction with Flowfield

The temperature contour is shown for the time corresponding to the instantaneous initialization of high temperature filament for $\frac{L}{D} = 1.0$ and $\frac{\Delta T}{T_\infty} = 1.0$ (Figure 6.1(b)). Due to the instantaneous process of discharge the density is unchanged inside the filament and the pressure distribution is similar to the temperature profile.

Figure 6.2 presents the drag variation with respect to dimensionless time throughout the filament interaction and afterwards for $\frac{L}{D} = 1.0$ and $\frac{\Delta T}{T_\infty} = 1.0$. The dimensionless time is defined as

$$\tau = \frac{U_\infty}{D} t \tag{6.5}$$

where U_∞ is the velocity of the incoming flow, D the cylinder diameter, and t is the dimensional time. Therefore, when $\frac{L}{D} = 1.0$ and $\frac{\Delta T}{T_\infty} = 1.0$, the dimensionless time corresponds to the time required for the cylinder to move one filament length. The curve demonstrates a reduced drag once the filament travels completely into the bow shock ($\tau \approx 1$) and a further

[1]Figure reprinted with permission of the American Institute of Aeronautics and Astronautics

substantial reduction subsequently ($\tau \approx 5$) followed by the recovery phase. The highlighted points on this curve represent key features of the interaction process. The pressure contour and numerical schlieren images corresponding to the highlighted points on drag curve are shown in Figures 6.3 and 6.4 (for details on calculation and visualization of the numerical schlieren image, see sect. **??**).

Instantly after initialization of the heated filament in the flowfield, a blast wave is generated. The blast waves travels from the filament into the flowfield (see Figure 6.5). A series of expansion waves reflect back towards the centerline of the filament resulting in a pressure and temperature drop inside the filament. Upon relaxing of the filament pressure to the ambient pressure, the interaction nature becomes comparable with the studies of Azarova et al. [39] and Ganiev et al. [43, 45] (see sect. 3.4). Shock lensing occurs during the early stages of the interaction and the bow shock proceeds upstream gradually to a maximum stand-off distance before it begins moving backward. A contact surface is initially formed where the filament boundary and the bow shock meet. This is the source of a Richtmyer-Meshkov instability (Figures 6.3(a)-6.3(e)) which later develops into a toroidal vortex, moves off the axis, and passes the front face of the cylinder. During this course of interaction, the bow shock passes the original stand-off point moving towards the cylinder and reaches a minimum distance to the cylinder front face, where it then relaxes to the steady state position (Figure 6.4(e)).

The steady state drag coefficient is $C_{Ds} = 1.76$ (point 1 in Figure 6.2). Over the interaction time, the drag coefficient rises slightly and decreases to point 2 once the cylinder has moved forward one filament length (Figure 6.3(a)). The drag increases back to point 3 as a recirculation region is generated ahead of the cylinder behind the shock (Figure 6.3(c)). Point 4 indicates constant drag decrease on the curve and corresponds to the growing vortex phase as it moves off the axis towards the cylinder corner (Figure 6.3(e)).

The maximum drag reduction occurs at point 5 (Figure 6.4(a)) when the vortex has reached the corner of the cylinder. Beyond point 5, the toroidal vortex is drifted past the front face of the cylinder and at point 6, the drag continues to increase above the steady state value of point 1 (Figure 6.4(c)). This phenomenon is very analogous to dynamic stall in airfoils. The dynamic stall is a vortex shed above the airfoil towards the trailing edge

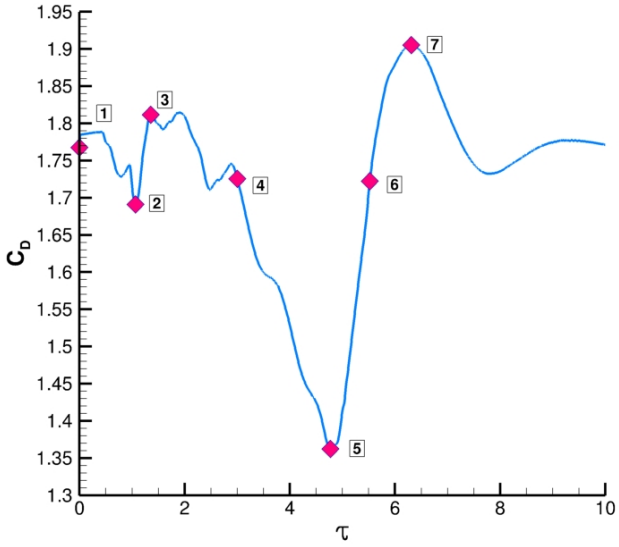

(a)

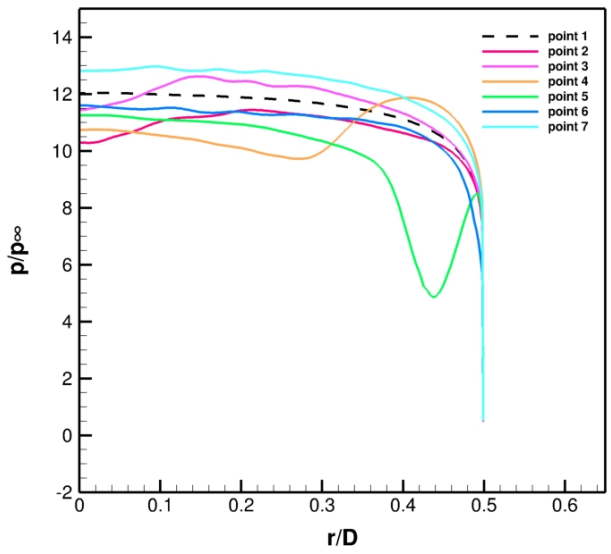

(b)

Figure 6.2: (a) Drag variation with respect to dimensionless time and (b) pressure curves on the front surface of the cylinder after introduction of the high temperature filament into the flowfield ($\frac{L}{D} = 1.0$)

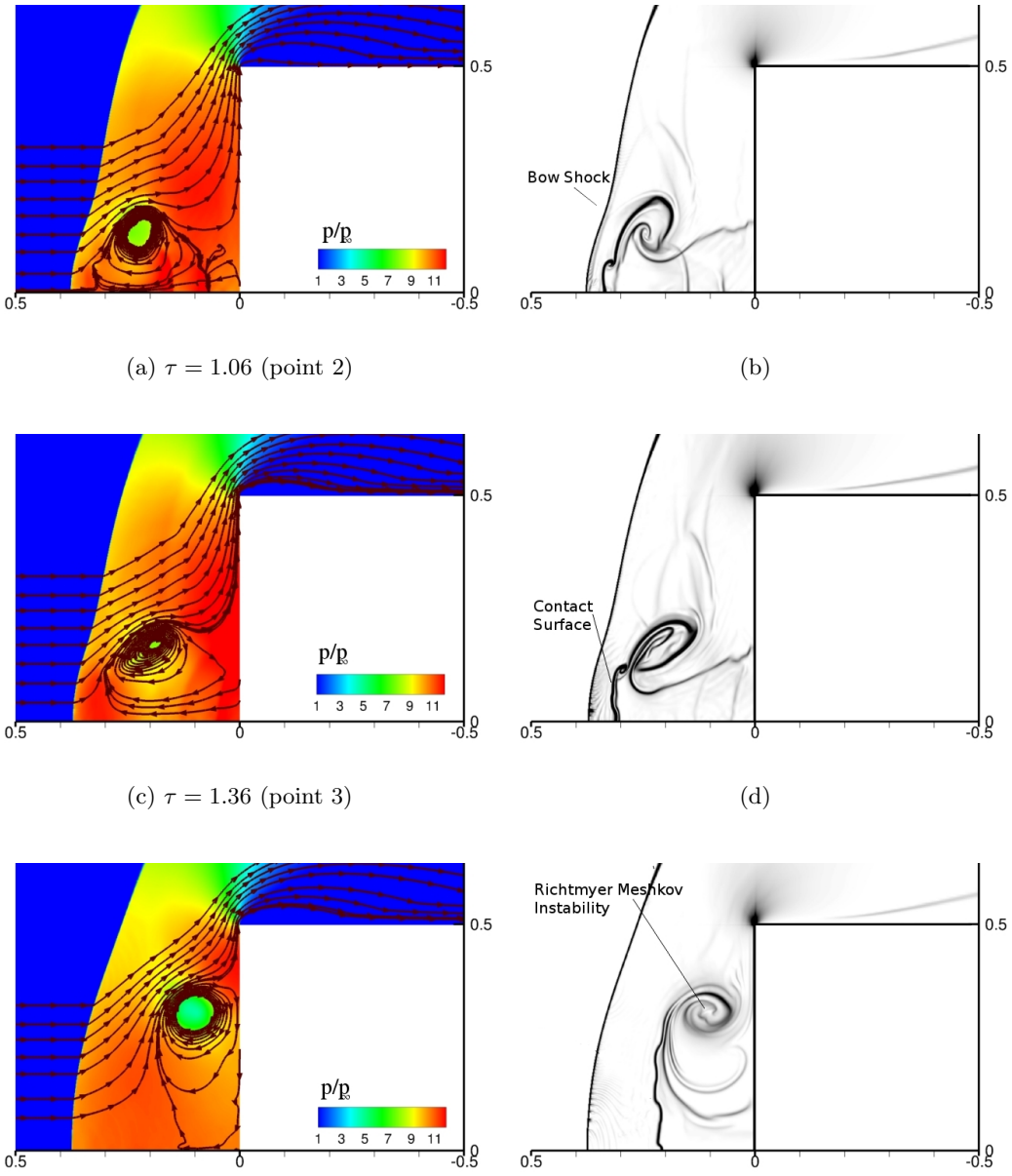

(a) $\tau = 1.06$ (point 2)

(b)

(c) $\tau = 1.36$ (point 3)

(d)

(e) $\tau = 3$ (point 4)

(f)

Figure 6.3: Pressure contours with instantaneous streamlines and numerical schlieren images of the flowfield at different dimensionless time intervals, $\frac{L}{D} = 1.0$ and $\frac{\Delta T}{T_\infty} = 1.0$ ($\tau = 1.06, 1.36, 3$)[8]

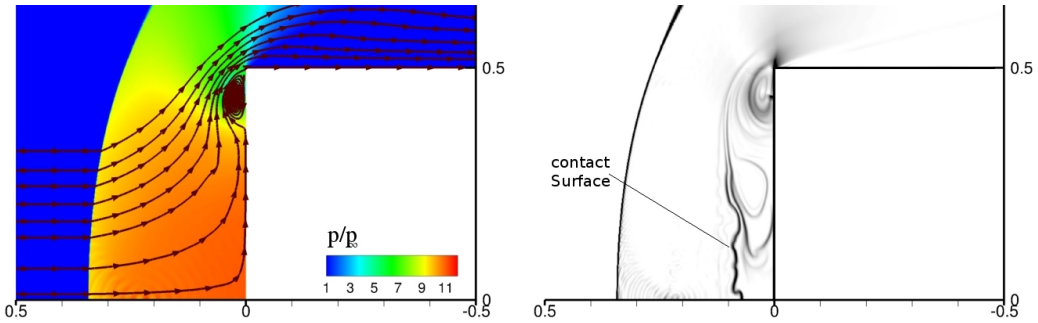

(a) $\tau = 4.77$ (point 5) (b)

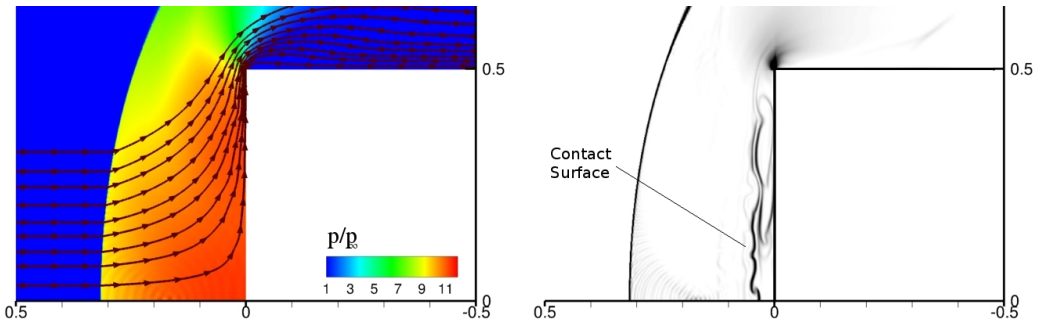

(c) $\tau = 5.54$ (point 6) (d)

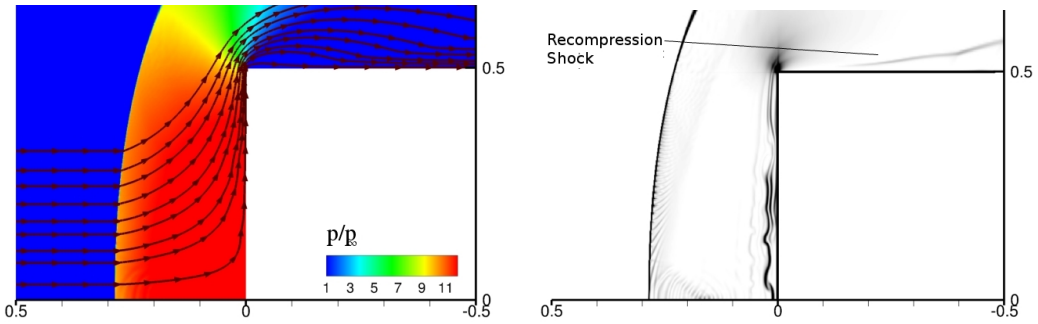

(e) $\tau = 6.33$ (point 7) (f)

Figure 6.4: Pressure contours with instantaneous streamlines and numerical schlieren images of the flowfield at different dimensionless time intervals, $L/D = 1.0$ and $\frac{\Delta T}{T_\infty} = 1.0$ ($\tau = 4.77, 5.54, 6.33$)[8]

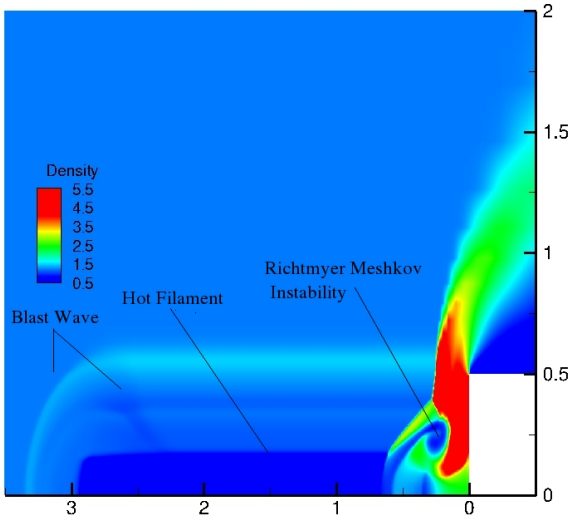

Figure 6.5: Formation of the blast wave immediately after initialization of the high temperature filament, $\frac{L}{D} = 4.0$ and $\frac{\Delta T}{T_\infty} = 5.0$

and forms due to a sudden change in angle of attack. The vortex above the airfoil disturbs the steady state pressure distribution above which leads to a sudden increase in lift. The lift force drops significantly as the vortex passes the trailing edge [56].

It is noteworthy that drag reduction in energy deposited systems has been seen to occur due to a different phenomenology [47]. Azarova et al. noticed significant drag reduction after formation of a vortex which resulted in the stagnation point movement off the front face [57, 39]. By contrast, in the current study, the stagnation point remains on the front face (Figure 6.4(a)). Kolesnichenko et al. indicated the body streamlining effect from vortex formation as the underlying mechanism of drag reduction in a similar system [4]. By contrast, in the current study there is no body streamlining effect at the moment of minimum drag (Figure 6.4(a)). Finally, at point 7 (Figure 6.4(e)), the bow shock moves towards the minimum distance from the cylinder front face. The steady state drag is recovered as the bow shock relaxes back to the initial location.

Figure 6.6 shows the drag coefficient curve for $\frac{L}{D} = 4.0$ and $\frac{\Delta T}{T_\infty} = 11.0$. Three specific points on the drag curve along with the corresponding instantaneous streamlines and Mach contours and the numerical schlieren images are presented in Figure 6.7. Formation of a

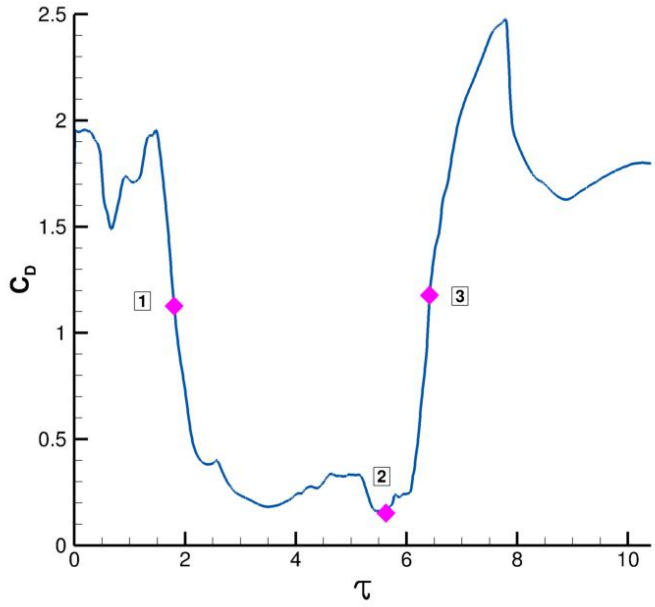

Figure 6.6: Drag reduction *vs.* dimensionless time for $\frac{L}{D} = 4.0$ and $\frac{\Delta T}{T_\infty} = 11.0$

Richtmyer-Meshkov instability and development of the toroidal vortex ahead of the cylinder result in a minimum drag at point 2 ($\tau = 5.6$). In an earlier study, it has been shown that the minimum drag for $\frac{\Delta T}{T_\infty} = 1.0$ happens upon arrival of the vortex on the corner of the cylinder [8]. In the present research, it is seen that the toroidal vortex moves back towards the axis once it reaches the corner and it bounces in between for a while. This phenomenon can justify the longer time interval over which the drag coefficient remains close to the minimum. Moreover, a second shock is generated behind the initial bow shock as the maximum added temperature inside the filament is increased.

6.3 Drag Reduction Trend

The drag variation results are presented from the two different perspectives of various filament length and temperature.

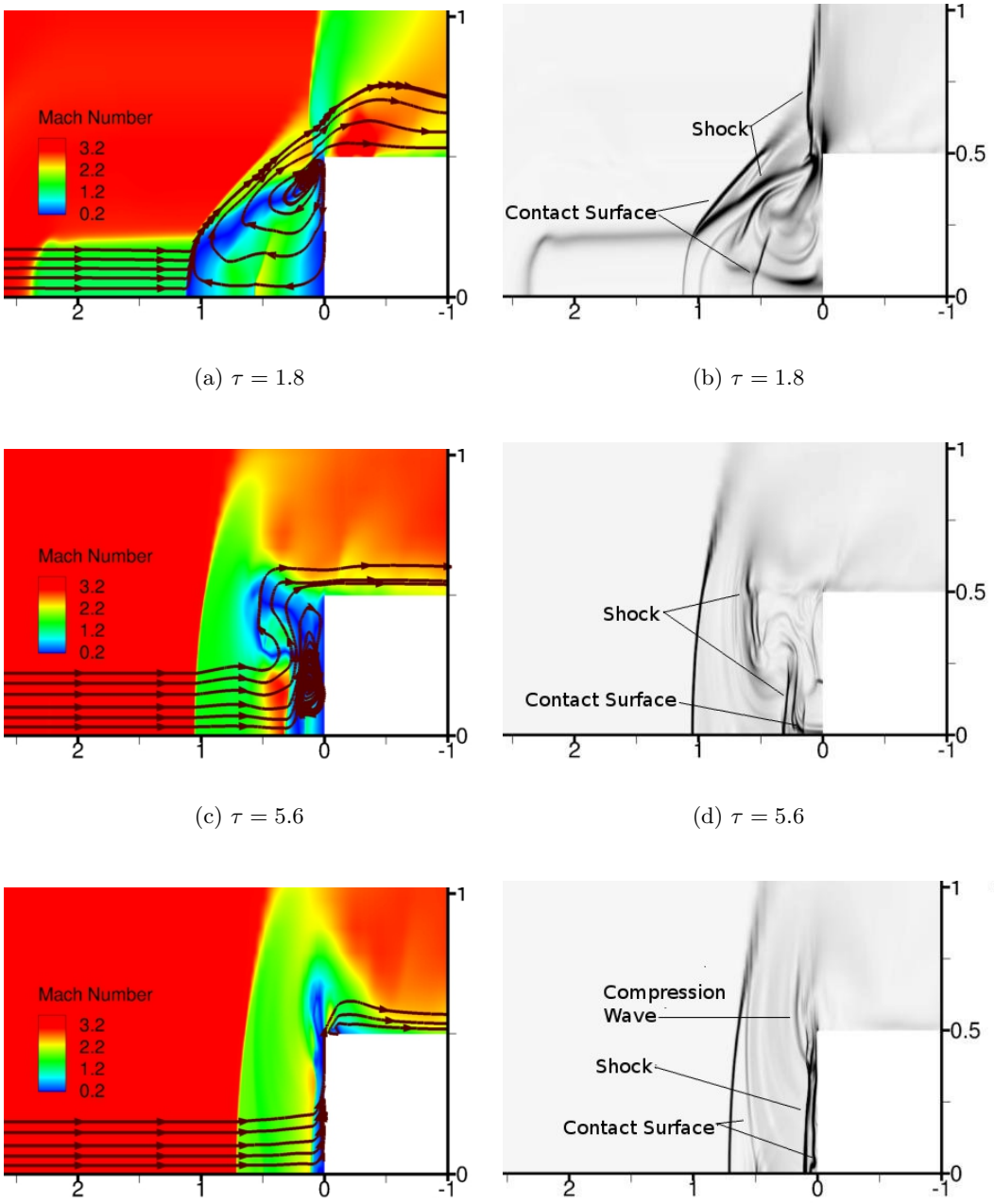

(a) $\tau = 1.8$

(b) $\tau = 1.8$

(c) $\tau = 5.6$

(d) $\tau = 5.6$

(e) $\tau = 6.4$

(f) $\tau = 6.4$

Figure 6.7: Interaction of the heated filament with the flowfield: Formation of Richtmyer-Meshkov instability and development of the toroidal vortex at three dimensionless time intervals for $\frac{L}{D} = 4.0$ and $\frac{\Delta T}{T_\infty} = 11.0$ ($\tau = \frac{U_\infty t}{D}$)

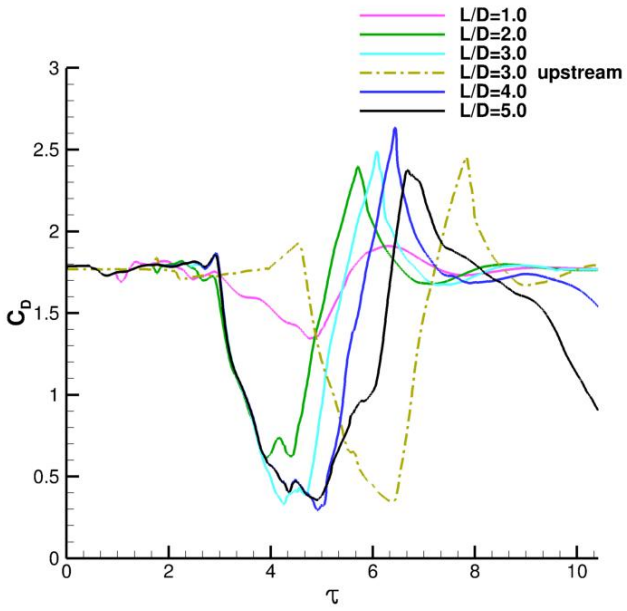

Figure 6.8: Drag reduction *vs.* dimensionless time for all filament length configurations, $\frac{\Delta T}{T_\infty} = 1.0$

6.3.1 Filament Length Effect

Figure 6.8 presents the drag coefficient curve results obtained from Richardson extrapolation (see sect. 5) for five different filament lengths and a sixth configuration where the filament is inserted upstream of the bow shock. A noticeable change in the momentary minimum drag is observed with increasing filament length from $\frac{L}{D} = 1.0$ to 2.0. Nevertheless, the drag reduction becomes asymptotic with higher filament lengths of $\frac{L}{D} = 3.0$ to $\frac{L}{D} = 5.0$. In addition, for the filament length of $\frac{L}{D} = 5.0$, a considerable pulsating effect (a secondary drag reduction before recovery) is observed. The pulsating effect is similarly seen in Azarova's calculations with infinitely long rarefied filaments [57]. The two drag curves for $L/D = 3.0$ and $L/D = 3.0$ *upstream* exhibit a very similar behavior except for the time delay for upstream filament to reach the bow shock before interaction.

6.3.2 Filament Temperature Effect

Figure 6.9 presents the drag curve results obtained from Richardson extrapolation (see sect. 5) for the total six cases of different filament temperatures. Likewise, a non-linear trend holds for maximum drag reduction with temperature increase. A drop in minimum

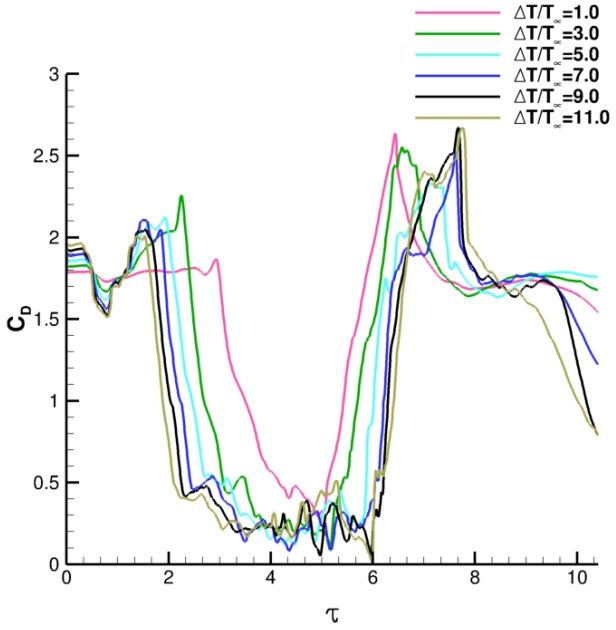

Figure 6.9: Drag reduction *vs.* dimensionless time for all filament temperature cases, $\frac{L}{D} = 4.0$

drag coefficient is observed from $\frac{\Delta T}{T_\infty} = 1.0$ to $\frac{\Delta T}{T_\infty} = 3.0$. The drag reduction asymptotes with higher magnitudes of temperature increase in the filament. A pulsating effect exists for cases of $\frac{\Delta T}{T_\infty} > 5.0$.

6.4 Efficiency

Efficiency is the ratio of the energy saved from drag reduction by the heated filament to the invested energy in the filament. Therefore, from Eq. (3.13)

$$\eta = \frac{\Delta E_{saved}}{\Delta E_{invested}} = \frac{\int_0^{t_f}\int_0^{2\pi}\int_0^{D/2} U_\infty [p_0(r) - p_f(r,t)] r dr d\theta dt}{\int_V \rho_s c_v \Delta T e^{-(r/r_\circ)^2} dV} \tag{6.6}$$

where $U_\infty, t_f, p_0(r)$ and $p_f(r,t)$ are incoming flow velocity, the interaction time period of the filament with the flowfield, undisturbed frontal pressure distribution and modified frontal pressure distribution due to heated filament, respectively.

Figures 6.10 and 6.11 present the values of efficiency for all various computational configurations. The results for constant filament temperature imply a dramatic increase in efficiency from $\frac{L}{D} = 1.0$ to $\frac{L}{D} = 2.0$ and a asymptotic increase in efficiency with higher filament lengths. A higher efficiency is achieved for the filament when it is inserted upstream

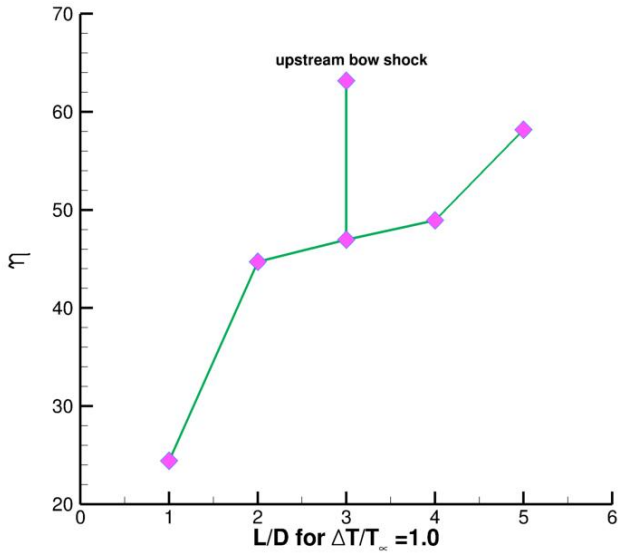

Figure 6.10: Efficiency values for all filament length configurations, $\frac{\Delta T}{T_\infty} = 1.0$

of the bow shock. In contrary, at constant filament length, the efficiency values decrease asymptotically with higher temperatures.

6.5 Effectiveness

Effectiveness is the ratio of the average drag reduction by heated filament to the undisturbed drag

$$\zeta = \frac{\int_0^{t_f} \int_0^{2\pi} \int_0^{D/2} [p_0(r) - p_f(r,t)] r dr d\theta dt}{\int_0^{t_f} \int_A p_0(r) dr d\theta dt} \tag{6.7}$$

where $p_0(r)$ and $p_f(r,t)$ are frontal pressure distribution in absence and presence of the heated filament respectively. Figures 6.12 and 6.13 presents the values of effectiveness for all configurations. The graphs indicate a moderate increase for effectiveness with higher values of filament length and temperature which can be attributed to the formation of secondary vortex and pulsating effect.

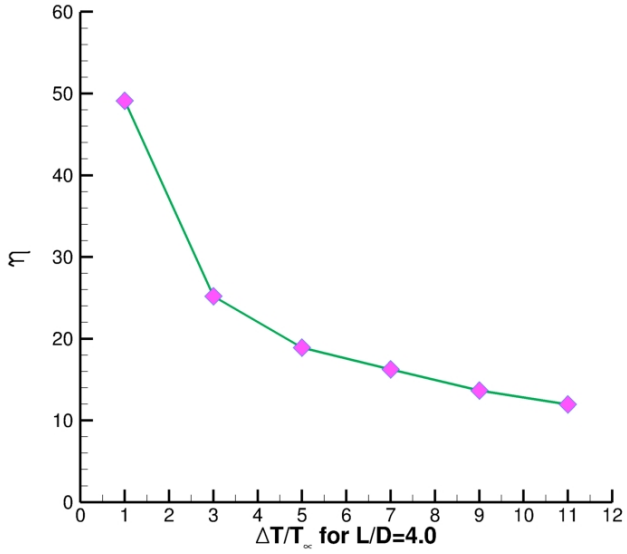

Figure 6.11: Efficiency values for all filament temperature cases, $\frac{L}{D} = 4.0$

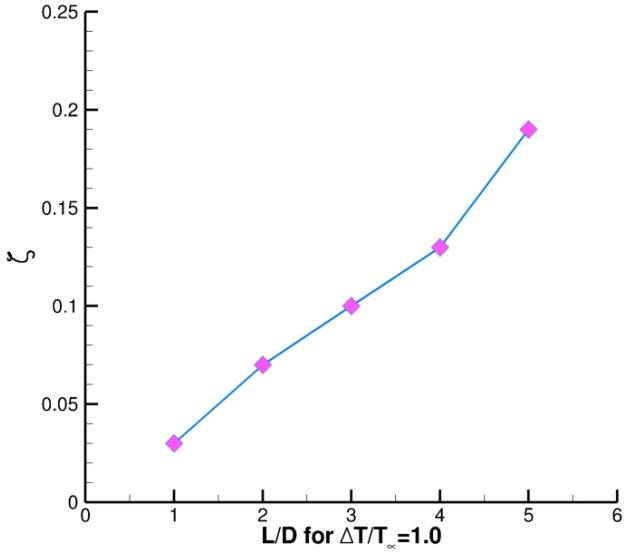

Figure 6.12: Effectiveness values for all filament length configurations, $\frac{\Delta T}{T_\infty} = 1.0$

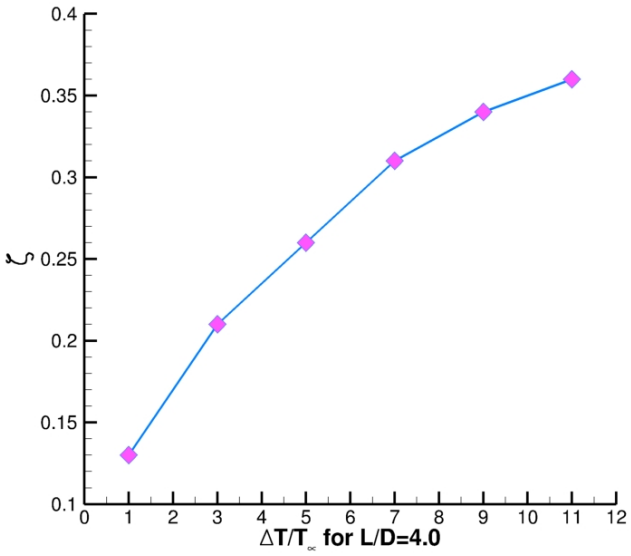

Figure 6.13: Effectiveness values for all filament temperature cases, $\frac{L}{D} = 4.0$

6.6 Analytical Results

Figure 6.14 presents both analytical and numerical results for the ratio of the dimensionless disturbed to the undisturbed pressure as a function of $\frac{\Delta T}{T_0}$ for $M_0 = 3.0$, $\frac{L}{D} = 4.0$ and $\gamma = 1.4$.

The analytical curve indicates an asymptotic reduction in pressure decrease of a fluid particle lying on a pathline close to the axis and front face of the cylinder. The analytical results indicate an asymptotic behavior for maximum pressure drop at a point on the corner of the cylinder close to the sonic line as the maximum temperature in the filament increases.

The numerical points present the average minimum pressure and the corresponding standard deviation on the front face of the cylinder. The minimum pressure is averaged over the time $\tau = 2.0$ to $\tau = 6.0$ when minimum drag occurs for most of the different filament temperatures (see Figure 6.9).

Comparing the analytical and numerical results reveals the fact that the average minimum pressure values are close to the theoretical curve for higher filament temperatures while discrepancies are observed for the first two cases, *i.e.*, $\frac{\Delta T}{T_\infty} = 1.0, 3.0$ due to occurrence

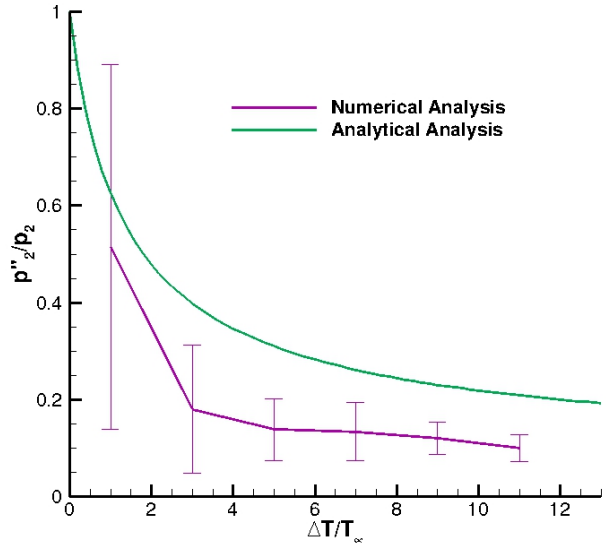

Figure 6.14: Asymptotic pressure reduction on the front face of the cylinder at $M = 3$

of drag reduction in a smaller time frame. It is worth to mention that the analytical pressure curve can verify the asymptotic trend of the computational graphs in Fig. 6.8 and 6.9 since they both represent higher energy deposition magnitudes.

Chapter 7

Conclusions

Interaction of a heated filament with blunt cylinder at Mach 3 is numerically simulated. In a dimensionless configuration, 12 cases have been computed, *i.e.*, 5 different filament lengths and 6 different filament temperatures where the filaments intersect the bow shock and one case where the filament is located upstream of the bow shock. A one-dimensional analytical analysis also shows similar trends to the aforementioned asymptotic results from numerical calculations. The results for computational simulation of various heated filaments ahead of a blunt cylinder at Mach 3 reveals the following conclusions: 1) a Richtmyer-Meshkov instability develops a toroidal vortex ahead of the cylinder due to instantaneous initiation of the filament which results in significant drag reduction, 2) the minimum drag occurs when the toroidal vortex is close to the corner of the cylinder, 3) a saturation effect is observed on the maximum drag reduction with higher filament length and temperature, 4) a pulsating effect (secondary drag reduction) is resulted as the temperature and length of the filament is increased, 5) the location of the filament on the axis does not impact the drag reduction, 6) the efficiency increases with longer filaments, and 7) the effectiveness increases with higher filament length and temperature.

The above research findings as well as an analytical validation are published in [58].

Chapter 8

Appendix

Schlieren imaging is the technique implemented to visualize the density inhomogeneities in transparent media. In high speed flow regimes, the density variations correspond to compression and expansion waves. In practice, a collimated source illuminates a section of the flow. The collimated beam is distorted due to different refractive index in flow with varying density gradients. A shadowgraph system can capture the various intensity light shined on the flow. In this system the second derivative of the density is measured. In addition to the shadowgraph system, a schlieren imaging system can also capture the density gradient of the flow. This system captures the first derivative of the density. In this method, a schlieren image is created by use a convex lens and a knife edge. A source point is using illuminate the test section area. A convex lens is used to generate an image of the test section and the source point. From the thin lenses theory

$$\frac{1}{f} = \frac{1}{d_o} + \frac{1}{d_i} \tag{8.1}$$

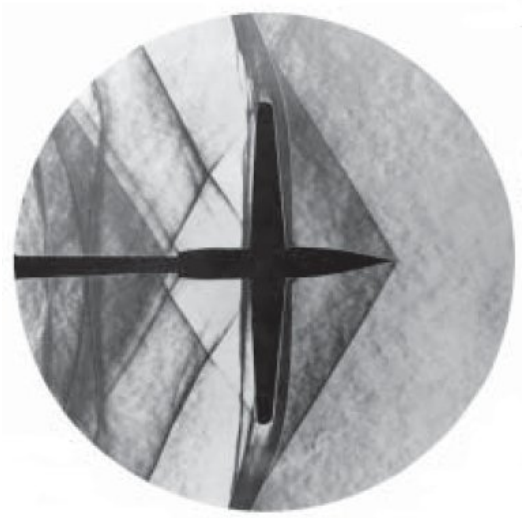

Figure 8.1: A schlieren image representing compression ahead of a Mach 1.2 wing. (Figure reprinted from http://en.wikipedia.org/wiki/Schlieren_photography)

where f is the focal length of the lens, d_i is the distance between the image and the lens, and d_o is the distance between the object and the lens. A knife edge is then placed on the focal point to partially block the source point. If the flow density is uniform, the image would reflect a blocked area of light. However, if there exists a density gradient in the flow test section, lighter and darker patches are created which are corresponded to positive and negative density gradients, respectively. Figure 8.1 shows a schlieren photograph of the compression in front of a wing at Mach 1.2.

To post-process the results of a computational simulation of a flow domain and generate a numerical schlieren image, the flow parameters are imported to Tecplot once the solution is complete. The flow parameters required to this process include geometrical coordinates X, Y, Z, velocity components U, V, W, and two of the thermodynamics parameters (pressure, temperature, and density). The magnitude of the density gradient which consists of all density gradient components in three dimensions can be calculated using the Flow Analysis menu in Tecplot [54]. To visualize the density gradients similar to measured schlieren images, a gray scale contour plot of the the density gradient magnitude in addition to adjustment of cut-off limits in the flowfield is required.

References

http://en.wikipedia.org/wiki/Schlieren_photography

http://en.wikipedia.org/wiki/Schlieren

Bibliography

[1] Knight, D. and Kolesnichenko, U., "High Speed Flow Control Using Microwave and Laser Discharge," Lecture Series Notes, von Karman Institute for Fluid Dynamics, Brussels, Belgium, February 2011.

[2] Knight, D., Kuchinskiy, V., Kuranov, A., and Sheikin, E., "Aerodynamic Flow Control at High Speed Using Energy Deposition," *Fourth Workshop on Magneto-Plasma Aerodynamics for Aerospace Applications, Institute for High Temperatures, Russian Academy of Sciences, Moscow*, April, 9-11, 2002.

[3] Bletzinger, P., Ganguly, B., Van Wie, D., and Garscadden, A., "Plasmas in High Speed Aerodynamics," *Journal of Physics D: Applied Physics*, Vol. 38, 2005, pp. R33–R57.

[4] Kolesnichenko, Y., Brovkin, V., Azarova, O., Grudnitsky, V., Lashkov, V., and Mashek, I., "Microwave Energy Release Regimes for Drag Reduction in Supersonic Flow," AIAA Paper 2002-0353, American Institute of Aeronautics and Astronautics, January 2002.

[5] Fomin, V., Tretyakov, P., and Taran, J.-P., "Flow Control Using Various Plasma and Aerodynamic Approaches (Short Review)," *Aerospace Science and Technology*, Vol. 8, 2004, pp. 411–421.

[6] Knight, D., "Survey of Aerodynamic Drag Reduction at High Speed by Energy Deposition," *Journal of Propulsion and Power*, Vol. 24, No. 6, November-December 2008, pp. 1153–1167.

[7] Ogino, Y., Ohnishi, N., Taguchi, S., and Sawada, K., "Baroclinic Vortex Influence on Wave Drag Reduction Induced by Pulse Energy Deposition," *Physics of Fluids*, Vol. 21, No. 066102, 2009, pp. 1–11.

[8] Golbabaei-Asl, M. and Knight, D., "Interaction of High Temperature Filament with

Blunt Cylinder at Mach 3," AIAA Paper 2012-1026, American Institute of Aeronautics and Astronautics, 2012.

[9] Giammanco, F., Giulietti, A., Vaselli, M., and Einaudi, G., "An Evolution Model for Laser-Produced Plasma. Theory and Experiment," *IL NUOVO CIMENTO*, Vol. 25 B, N. 2, August 1979, pp. 187–201.

[10] Yan, H., Adelgren, R., Boguszko, M., Elliott, G., and Knight, D., "Laser Energy Deposition in Quiescent Air," *AIAA Journal*, Vol. 11, 2003, pp. 1988–1995.

[11] Méchain, G., "Study of Filamentation of Femtosecond Laser Pulses in Air," Doctorate Thesis, École Polytechnique, Palaiseau, France, 2005.

[12] Couairon, A. and Mysyrowicz, A., "Femtosecond Filamentation in Trasparent Media," *Physics Reports*, Vol. 441, 2007, pp. 47–189.

[13] Tzortzakis, S., Bergé, L., Couairion, A., Franco, M., Prade, B., and Mysyrowicz, A., "Break-up and Fusion of Self-Guided Femtosecond Light Pulses in Air," *Physics Review Letters*, Vol. 86, 2001, pp. 5470–5473.

[14] Khmara, D., Kolesnichenko, Y., and Knight, D., "Modeling of Microwave Filament Origination," AIAA Paper 2006-0794, American Institute of Aeronautics and Astronautics, January 2006.

[15] Kolesnichenko, Y., "Microwave Discharge in Free Space," Thematic Workshop on Fundamentals of Aerodynamic Flow and Combustion Control by Plasmas, Villa Monastero, Varenna, Italy, May 2007.

[16] Mashek, I., Anisimov, Y., and Lashkov, V., "Microwave Discharge Initiated by Laser Spark in Air," AIAA Paper 2004-0358, American Institute of Aeronautics and Astronautics, January 2004.

[17] "Optimization of Laser-Pulse-Controlled MW Energy Deposition," AIAA Paper 2007-1228, American Institute of Aeronautics and Astronautics, January 2007.

[18] Kolesnichenko, Y., Brovkin, V., and Khmara, D., "Laser-MW Energy Deposition in Air," Eucass paper, 2 nd European Conference for Aerospace and Sciences, Brussels, Belgium, 2007.

[19] Bodrov, S., Kulagin, D., Malkov, Y., Murzanev, A., Smirnov, A., and Stepanov, A., "Initiation and Channelling of a Microwave Discharge by a Plasma Filament Created in Atmospheric Air by an Intense Femtosecond Laser Pulse," *Journal of Physics D: Applied Physics*, Vol. 45, january 2012, pp. 045202.

[20] Miles, R., "Plasma Flow Control, Fundamentals, Modeling, and Applications," Lecture Series Notes, von Karman Institute for Fluid Dynamics, Brussels, Belgium, February 2011.

[21] Adelgren, R., Elliott, G., Knight, D., Zheltovodov, A., and Beutner, T., "Energy Deposition in Supersonic Flows," AIAA Paper 2001-0885, American Institute of Aeronautics and Astronautics, January 2001.

[22] Adelgren, R., Boguszko, M., and Elliott, G., "Experimental Summary Report – Shock Propagation Measurements for Nd:YAG Laser Induced Breakdown in Quiescent Air," *Dept of Mechanical and Aerospace Engineering, Rutgers University, October*, 2001.

[23] Adelgren, R., Elliott, G., Knight, D., and Ivanov, M., "Preliminary Study of Localized Pulsed Laser Energy Deposition Effects on Shock Structures in Mach/Regular Reflection Dual Solution Domain at Mach 3.45," *Report RU-TR-MAE-213, Dept of Mechanical and Aerospace Engineering, Rutgers University, July*, 2001.

[24] Mori, K., Komurasaki, K., and Arakawa, Y., "Laser Plasma Production and Explosion in a Supersonic Flow," AIAA Paper 2002-0634, American Institute of Aeronautics and Astronautics, January 2002.

[25] Kremeyer, K., "Lines of Pulsed Energy for Supersonic/Hypersonic Drag Reduction: Generation and Implementation," AIAA Paper 2004-984, American Institute of Aeronautics and Astronautics, 2004.

[26] Adelgren, R., Yan, H., Elliott, G., Knight, D., Beutner, T., and Zheltovodov, A., "Control of Edney IV Interaction by Pulsed Laser Energy Deposition," *AIAA Journal*, Vol. 43, No. 2, 2005, pp. 256–269.

[27] Girgis, I., Shneider, M., Macheret, S., Brown, G., and Miles, R., "Steering Moments Creation in Supersonic Flow by Off-Axis Plasma Heat Addition," *Journal of Spacecraft and Rocket*, Vol. 43, No. 3, May-June 2006, pp. 607–613.

[28] Sasoh, A., Ohtani, T., and Mori, K., "Pressure Effect in a Shock-Wave Plasma Interaction Induced by a Focused Laser Pulse," *Physical Review Letters - The American Physical Society*, Vol. PRL 97, 2006, pp. 205004.

[29] Kandala, R. and Candler, G., "Numerical Studies of Laser-Induced Energy Deposition for Supersonic Flow Control," *AIAA Journal*, Vol. 42, No. 11, 2004, pp. 2266–2275.

[30] Fornet, B., Dufour, G., and Rogier, F., "Interaction of Plasma and Incoming Flow at Mach 3," *Procedia Computer Science*, Vol. 1, No. 1, May 2010, pp. 617–626.

[31] Rogier, F., Dufour, G., and Fornet, B., "Numerical Modelling of Supersonic Flow Actuated by Laser-induced Plasma," AVT190 Meeting, NATO RTO AVT Panel Business Meeting, Edinburgh, UK, October 2011.

[32] Schulein, E., Zheltovodov, A., Pimonov, E., and Loginov, M., "Experimental and Numerical Modeling of the Bow Shock Interaction with Pulse-Heated Air Bubbles," *International Journal of Aerospace Innovations*, Vol. 2, 2010, pp. 165–187.

[33] Exton, R., Balla, R., Shirinzadeh, B., Brauckmann, G., Herring, G., Kelliher, W., Fugitt, J., Lazard, C., and Khodataev, K., "On-Board Projection of a Microwave Plasma Upstream of a Mach 6 Bow Shock," *Physics of Plasma*, Vol. 8, No. 11, November 2001, pp. 5013–5017.

[34] Azarova, O., Grudnitsky, V., and Kolesnichenko, Y., "Some Gas Dynamic Aspects of Flow Control by MW Energy Deposition," *Sixth Workshop on Magneto-Plasma-Aerodynamics for Aerospace Applications*, Institute for High Temperatures, Moscow, Russia, 2005, pp. 152–163.

[35] Ardelyan, N., Bychkov, V., and Malmuth, N., "Hot Filaments for Plasma Aerodynamic Applications," AIAA Paper 2007-1233, American Institute of Aeronautics and Astronautics, January 2007.

[36] Lashkov, V., Mashek, I., Anisimov, Y., Ivanov, V., Kolesnichenko, Y., and Azarova, A., "Gas Dynamic Effects Around the Body Under Energy Deposition in Supersonic Flow," AIAA Paper 2007-1231, American Institute of Aeronautics and Astronautics, January 2007.

[37] Knight, D., Kolesnichenko, Y., Brovkin, V., Khmara, D., Lashkov, V., and Mashek, I., "Interaction of Microwave-Generated Plasma with a Hemisphere Cylinder at Mach 2.1," *AIAA Journal*, Vol. 47, No. 12, December 2009, pp. 2996–3010.

[38] Azarova, O., Knight, D., and Kolesnichenko, Y., "Instabilities, Vortices and Structures Characteristics During Interaction of Microwave Filaments with Body in Supersonic Flow," AIAA Paper 2010-1004, American Institute of Aeronautics and Astronautics, January 2010.

[39] Azarova, O., Knight, D., and Kolesnichenko, Y., "Characterization of Flowfield Types initiated by Interaction of Microwave Filament with Supersonic Body," AIAA Paper 2011-1381, American Institute of Aeronautics and Astronautics, January 2011.

[40] Anderson, K. and Knight, D., "Interaction of Filaments with a Blunt Cylinder in Supersonic Flow," *Shock Waves*, Vol. 21, February 2011, pp. 149–161.

[41] Brovkin, V., Afanas'ev, S., Khmara, D., and Kolesnichenko, Y., "Experimental Investigation of Combined Laser-DC-MW Discharges," AIAA Paper 2006-1459, American Institute of Aeronautics and Astronautics, January 2006.

[42] Georgievsky, P. and Levin, V., "Modification of Regime of the Flow Over a Sphere by Means of Local Energy Supply Upstream," Proceedings Part 3, International Conference on the Methods of Aerophysical Research, Novosibirsk, Russia, September 1996.

[43] Ganiev, Y., Gordeev, V., Krasilnikov, A., Lagutin, V., Otmennikov, V., and Panasenko, A., "Theoretical and Experimental Study of the Possibility of Reducing Aerodynamic

Drag by Employing Plasma Injection," AIAA Paper A99-16474, International conference on the Methods of Aerophysical Research, January 1999.

[44] Ionikh, Y., Chernysheva, N., Meshchanov, A., Yalin, A., and Miles, R., "Direct Evidence for Thermal Mechanism of Plasma Influence on Shock Wave Propagation," *Physics Letters A*, Vol. 259, 1999, pp. 387–392.

[45] Ganiev, Y., Gordeev, V., Krasilnikov, A., Lagutin, V., Otmennikov, V., and Panasenko, A., "Aerodynamic Drag Reduction by Plasma and Hot-Gas Injection," *Journal of Thermophysics and Heat Transfer*, Vol. 14, No. 1, 2000, pp. 10–17.

[46] Georgievsky, P. and Levin, V., "Control of Flow Past Bodies Using Localized Energy Addition to the Supersonic Oncoming Flow," *Journal of Fluid Mechanics*, Vol. 38, No. 5, 2003, pp. 794–805.

[47] Georgievsky, P. and Levin, V., "Bow Shock Wave Structures Control by Pulse-Periodic Energy Input," AIAA Paper 2004-1019, American Institute of Aeronautics and Astronautics, January 2004.

[48] Kremeyer, K., Sebastian, K., and Shu, C., "Computational Study of Shock Mitigation and Drag Reduction by Pulsed Energy Lines," *AIAA Journal*, Vol. 44, No. 8, August 2006, pp. 1720–1731.

[49] *ICEM CFD Version 13.0 Reference Guide*, ANSYS Inc., Canonsburg, PA.

[50] Yan, H., Adelgren, R., Boguszko, M., Elliott, G., and Knight, D., "Laser Energy Deposition in Quiescent Air," AIAA Paper 2003-1051, American Institute of Aeronautics and Astronautics, January 2003.

[51] *GASPex Version 5 Reference Guide*, Aerosoft Inc., Blacksburg,VA.

[52] Knight, D., *Elements of Numerical Methods for Compressible Flows*, Cambridge University Press, New York, NY 10011-4211 USA, 2006.

[53] Harten, A., "High Resolution Schemes for Hyperbolic Conservation Laws," *Journal of Computational Physics*, Vol. 49, No. 3, March 1983, pp. 357–393.

[54] *Tecplot 360 Version 2013 Reference Guide*, Tecplot Inc., Bellevue, WA.

[55] Anderson, J., *Hypersonic and High Temperature Gas Dynamics*, AIAA Education Series, New York, US, 1989.

[56] Choudhuri, P. and Knight, D., "Two-Dimensional Unsteady Leading-Edge Separation on a Pitching Airfoil," *AIAA Journal*, Vol. 32, No. 4, 1994, pp. 673 – 681.

[57] Azarova, O., "Simulation of Stochastic Pulsating Flows with Instabilities Using Minimum-Stencil Difference Schemes," *Computational Mathematics and Mathematical Physics*, Vol. 49, 2009, pp. 1397–1414.

[58] Golbabaei-Asl, M. and Knight, D., "Numerical Characterization of High-temperature Filament Interaction with Blunt Cylinder at Mach 3," *Shock Waves*, Vol. 24, 2014, pp. 123–138.